# Sparse Unmixing of Hyperspectral Data

Marian-Daniel Iordache, José M. Bioucas-Dias, *Member, IEEE*, and Antonio Plaza, *Senior Member, IEEE*

***Abstract*—Linear spectral unmixing is a popular tool in remotely sensed hyperspectral data interpretation. It aims at estimating the fractional abundances of pure spectral signatures (also called as *endmembers*) in each mixed pixel collected by an imaging spectrometer. In many situations, the identification of the endmember signatures in the original data set may be challenging due to insufficient spatial resolution, mixtures happening at different scales, and unavailability of completely pure spectral signatures in the scene. However, the unmixing problem can also be approached in semisupervised fashion, i.e., by assuming that the observed image signatures can be expressed in the form of linear combinations of a number of pure spectral signatures known in advance (e.g., spectra collected on the ground by a field spectroradiometer). Unmixing then amounts to finding the optimal subset of signatures in a (potentially very large) spectral library that can best model each mixed pixel in the scene. In practice, this is a combinatorial problem which calls for efficient linear sparse regression (SR) techniques based on sparsity-inducing regularizers, since the number of endmembers participating in a mixed pixel is usually very small compared with the (ever-growing) dimensionality (and availability) of spectral libraries. Linear SR is an area of very active research, with strong links to compressed sensing, basis pursuit (BP), BP denoising, and matching pursuit. In this paper, we study the linear spectral unmixing problem under the light of recent theoretical results published in those referred to areas. Furthermore, we provide a comparison of several available and new linear SR algorithms, with the ultimate goal of analyzing their potential in solving the spectral unmixing problem by resorting to available spectral libraries. Our experimental results, conducted using both simulated and real hyperspectral data sets collected by the NASA Jet Propulsion Laboratory's Airborne Visible Infrared Imaging Spectrometer and spectral libraries publicly available from the U.S. Geological Survey, indicate the potential of SR techniques in the task of accurately characterizing the mixed pixels using the library spectra. This opens new perspectives for spectral unmixing, since the abundance estimation process no longer depends on the availability of pure spectral signatures in the input data nor on the capacity of a certain endmember extraction algorithm to identify such pure signatures.**

***Index Terms*—Abundance estimation, convex optimization, hyperspectral imaging, sparse regression (SR), spectral unmixing.**

Manuscript received March 14, 2010; revised August 18, 2010 and November 2, 2010; accepted November 28, 2010. Date of publication January 19, 2011; date of current version May 20, 2011. This work was supported by the European Community's Marie Curie Research Training Networks Program under contract MRTN-CT-2006-035927 (Hyperspectral Imaging Network) and by the Spanish Ministry of Science and Innovation (HYPERCOMP/EODIX project, reference AYA2008-05965-C04-02).

M.-D. Iordache and A. Plaza are with the Department of Technology of Computers and Communications, Escuela Politécnica, University of Extremadura, 10071 Cáceres, Spain (e-mail: diordache@unex.es; aplaza@unex.es).

J. M. Bioucas-Dias is with the Instituto de Telecomunicações, Instituto, Superior Técnico, 1049-1 Lisbon, Portugal (e-mail: bioucas@lx.it.pt).

Color versions of one or more of the figures in this paper are available online at http://ieeexplore.ieee.org.

Digital Object Identifier 10.1109/TGRS.2010.2098413

## I. Introduction

HYPERSPECTRAL imaging has been transformed from being a sparse research tool into a commodity product that is available to a broad user community [1]. The wealth of spectral information available from advanced hyperspectral imaging instruments currently in operation has opened new perspectives in many application domains, such as monitoring of environmental and urban processes or risk prevention and response, including, among others, tracking wildfires, detecting biological threats, and monitoring oil spills and other types of chemical contamination. Advanced hyperspectral instruments such as NASA's Airborne Visible Infrared Imaging Spectrometer (AVIRIS) [2] are now able to cover the wavelength region from 0.4 to 2.5 $\mu$m using more than 200 spectral channels at a nominal spectral resolution of 10 nm. The resulting hyperspectral data cube is a stack of images (see Fig. 1) in which each pixel (vector) is represented by a spectral signature or *fingerprint* that characterizes the underlying objects.

Several analytical tools have been developed for remotely sensed hyperspectral data processing in recent years, covering topics like dimensionality reduction, classification, data compression, or spectral unmixing [3], [4]. The underlying assumption governing clustering and classification techniques is that each pixel vector comprises the response of a single underlying material. However, if the spatial resolution of the sensor is not high enough to separate different materials, these can jointly occupy a single pixel. For instance, it is likely that the pixel collected over a vegetation area in Fig. 1 actually comprises a mixture of vegetation and soil. In this case, the measured spectrum may be decomposed into a linear combination of pure spectral signatures of soil and vegetation, weighted by abundance fractions that indicate the proportion of each *macroscopically* pure signature in the mixed pixel [5].

To deal with this problem, linear spectral mixture analysis techniques first identify a collection of spectrally pure constituent spectra, called as *endmembers* in the literature, and then express the measured spectrum of each mixed pixel as a linear combination of endmembers weighted by fractions or abundances that indicate the proportion of each endmember present in the pixel [6]. It should be noted that the linear mixture model assumes minimal secondary reflections and/or multiple scattering effects in the data collection procedure, and hence, the measured spectra can be expressed as a linear combination of the spectral signatures of the materials present in the mixed pixel [see Fig. 2(a)]. Being quite opposite, the nonlinear mixture model assumes that the endmembers form an intimate mixture inside the respective pixel so that the incident radiation interacts with more than one component and is affected by multiple scattering effects [see Fig. 2(b)]. Nonlinear unmixing generally

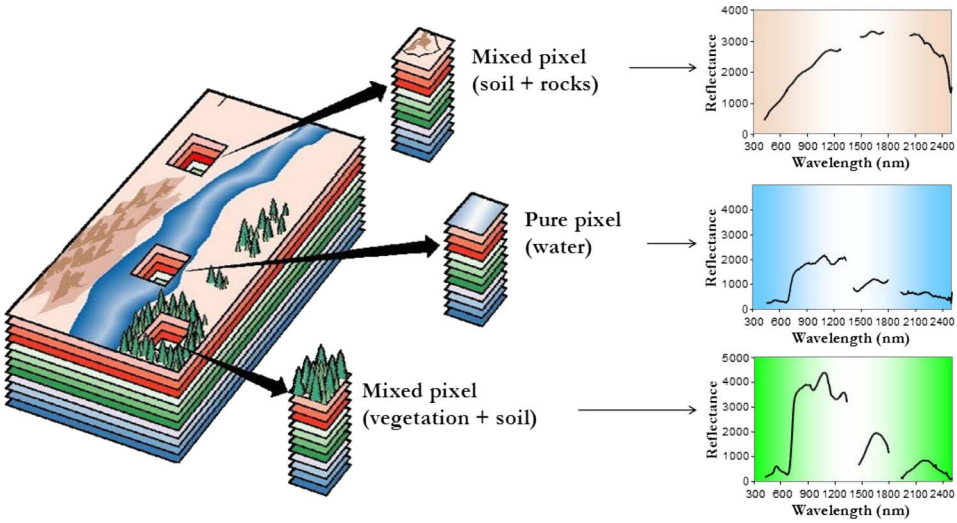


Fig. 1. Concept of hyperspectral imaging and the presence of mixed pixels.

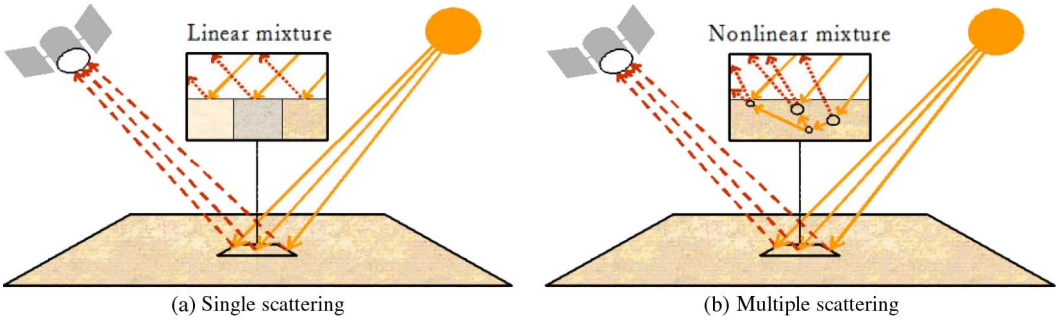


Fig. 2. (a) Linear versus (b) nonlinear mixture models.

requires prior knowledge about object geometry and the physical properties of the observed objects. In this paper, we will focus exclusively on the linear mixture model due to its computational tractability and flexibility in different applications.

The linear mixture model assumes that the spectral response of a pixel in any given spectral band is a linear combination of all of the endmembers present in the pixel at the respective spectral band. For each pixel, the linear model can be written as follows:

$$y_i = \sum_{j=1}^{q} m_{ij}\alpha_j + n_i \tag{1}$$

where $y_i$ is the measured value of the reflectance at spectral band $i$, $m_{ij}$ is the reflectance of the $j$th endmember at spectral band $i$, $\alpha_j$ is the fractional abundance of the $j$th endmember, and $n_i$ represents the error term for the spectral band $i$ (i.e., the noise affecting the measurement process). If we assume that the hyperspectral sensor used in data acquisition has $L$ spectral bands, (1) can be rewritten in compact matrix form as

$$\mathbf{y} = \mathbf{M}\boldsymbol{\alpha} + \mathbf{n} \tag{2}$$

where $\mathbf{y}$ is an $L \times 1$ column vector (the measured spectrum of the pixel), $\mathbf{M}$ is an $L \times q$ matrix containing $q$ pure spectral signatures (endmembers), $\boldsymbol{\alpha}$ is a $q \times 1$ vector containing the fractional abundances of the endmembers, and $\mathbf{n}$ is an $L \times 1$ vector collecting the errors affecting the measurements at each spectral band. The so-called abundance nonnegativity constraint (ANC) ($\alpha_i \geq 0$ for $i = 1, \ldots, q$) and the abundance sum-to-one constraint (ASC) ($\sum_{i=1}^{q} \alpha_i = 1$), which we, respectively, represent in compact form by

$$\boldsymbol{\alpha} \geq \mathbf{0} \tag{3}$$

$$\mathbf{1}^T\boldsymbol{\alpha} = 1 \tag{4}$$

where $\mathbf{1^T}$ is a line vector of 1's compatible with $\boldsymbol{\alpha}$, are often imposed into the model described in (1) [7], owing to the fact that $\alpha_i$, for $i = 1, \ldots, q$, represents the fractions of the endmembers present in the considered pixel.

In a typical hyperspectral unmixing scenario, we are given a set $\mathbf{Y} \equiv \{\mathbf{y}_i \in \mathbb{R}^L, i = 1, \ldots, n\}$ of $n$ observed $L$-dimensional spectral vectors, and the objective is to estimate the mixing matrix $\mathbf{M}$ and the fractional abundances $\boldsymbol{\alpha}$ for every pixel in the scene. This is a blind source separation problem, and naturally, independent component analysis methods come to mind to solve it. However, the assumption of statistical independence among the sources (the fractional abundances in our application), central to independent component analysis methods, does not hold in hyperspectral applications, since the sum of fractional abundances associated to each pixel is constant. Thus, the sources are statistically dependent, which compromises the performance of independent component analysis algorithms in hyperspectral unmixing [8].

We note that the constraints (3) and (4) define the set $\mathcal{S}_{q-1} \equiv \{\boldsymbol{\alpha} \in \mathbb{R}^q | \boldsymbol{\alpha} \geq \mathbf{0}, \mathbf{1}^T \boldsymbol{\alpha} = 1\}$, which is the probability simplex in $\mathbb{R}^q$. Furthermore, the set $\mathcal{S}_M \equiv \{\mathbf{M}\boldsymbol{\alpha} \in \mathbb{R}^L | \boldsymbol{\alpha} \in \mathcal{S}_{q-1}\}$ is also a simplex whose vertices are the columns of $\mathbf{M}$. Over the last decade, several algorithms have exploited this geometrical property by estimating the "smallest" simplex set containing the observed spectral vectors [9], [10]. Some classic techniques for this purpose assume that the input data set contains at least one pure pixel for each distinct material present in the scene, and therefore, a search procedure aimed at finding the most spectrally pure signatures in the input scene is feasible. Among the *endmember extraction* algorithms working under this regime, we can list some popular approaches such as the pixel purity index [11], N-FINDR [12], orthogonal subspace projection technique in [13], and vertex component analysis (VCA) [14]. However, the assumption under which these algorithms perform may be difficult to guarantee in practical applications due to several reasons.

1) First, if the spatial resolution of the sensor is not high enough to separate different pure signature classes at a macroscopic level, the resulting spectral measurement can be a composite of individual pure spectra which correspond to materials that jointly occupy a single pixel. In this case, the use of image-derived endmembers may not result in accurate fractional abundance estimations since it is likely that such endmembers may not be completely pure in nature.
2) Second, mixed pixels can also result when distinct materials are combined into a microscopic (intimate) mixture, independent from the spatial resolution of the sensor. Since the mixtures in this situation happen at the particle level, the use of image-derived spectral endmembers cannot accurately characterize intimate spectral mixtures.

In order to overcome the two aforementioned issues, other advanced *endmember generation* algorithms have also been proposed under the assumption that pure signatures are not present in the input data. Such techniques include optical real-time adaptive spectral identification systems [15], convex cone analysis [16], iterative error analysis [17], automatic morphological endmember extraction [18], iterated constrained endmembers (ICE) [19], minimum volume constrained nonnegative matrix factorization [20], spatial–spectral endmember extraction [21], sparsity-promoting ICE [22], minimum volume simplex analysis [23], and simplex identification *via* split augmented Lagrangian [24]. A necessary condition for these endmember generation techniques to yield good estimates is the presence in the data set of at least $q-1$ spectral vectors on each facet of the simplex set $\mathcal{S}_M$ [24]. This condition is very likely to fail in highly mixed scenarios, in which the aforementioned techniques generate *artificial* endmembers, i.e., not necessarily associated to physically meaningful spectral signatures of true materials.

In this paper, we adopt a novel semisupervised approach to linear spectral unmixing, which relies on the increasing availability of spectral libraries of materials measured on the ground, e.g., using advanced field spectroradiometers. Our main assumption is that mixed pixels can be expressed in the form of linear combinations of a number of pure spectral signatures known in advance and available in a library, such as a the well-known one publicly available from the U.S. Geological Survey (USGS),[1] which contains over 1300 mineral signatures, or the NASA Jet Propulstion Laboratory's Advanced Spaceborne Thermal Emission and Reflection Radiometer (ASTER) spectral library,[2] which is a compilation of over 2400 spectra of natural and man-made materials. When the unmixing problem is approached using spectral libraries, the abundance estimation process no longer depends on the availability of pure spectral signatures in the input data nor on the capacity of a certain endmember extraction algorithm to identify such pure signatures. Being quite opposite, the procedure is reduced to finding the optimal subset of signatures in the library that can best model each mixed pixel in the scene. Despite the appeal of this semisupervised approach to spectral unmixing, this approach is also subject to a few potential drawbacks.

1) One risk in using library endmembers is that these spectra are rarely acquired under the same conditions as the airborne data. Image endmembers have the advantage of being collected at the same scale as the data, and thus, they can be more easily associated with features on the scene. However, such image endmembers may not always be present in the input data. In this paper, we rely on the use of advanced atmospheric correction algorithms which convert the input hyperspectral data from at-sensor radiance to reflectance units.
2) The ability to obtain useful sparse solutions for an underdetermined system of equations mostly depends on the degree of coherence between the columns of the system matrix and the degree of sparseness of the original signals (i.e., the abundance fractions) [25]–[28]. The most favorable scenarios correspond to highly sparse signals and system matrices with low coherence. Unfortunately, in hyperspectral applications, the spectral signatures of the materials tend to be highly correlated. On the other hand, the number of materials present in a given scene is often small, e.g., less than 20, and most importantly, the number of materials participating in a mixed pixel is usually on the order of four to five [5]. Therefore, the undesirable high coherence of hyperspectral libraries can be mitigated, to some extent, by the highly sparse nature of the original signals.
3) The sparse solutions of the underdetermined systems are computed by solving the optimization problems containing nonsmooth terms [26]. The presence of these terms introduces complexity because the standard optimization tools of the gradient and Newton family cannot be directly used. To make the scenario even more complex, a typical hyperspectral image has hundreds or thousands of spectral vectors, implying an equal number of independent optimizations to unmix the complete scene. To cope up with this computational complexity, we resort to recently introduced (fast) algorithms based on the augmented Lagrangian method of multipliers [29].

[1] Available online at http://speclab.cr.usgs.gov/spectral-lib.html.
[2] Available online at http://speclib.jpl.nasa.gov.

In this paper, we specifically address the problem of sparsity when unmixing the hyperspectral data sets using spectral libraries and further provide a quantitative and comparative assessment of several available and new optimization algorithms in the context of linear sparse problems. The remainder of this paper is organized as follows. Section II formulates the sparse regression (SR) problem in the context of hyperspectral unmixing. Section III describes several available and new unmixing algorithms, with the ultimate goal of analyzing their potential in solving the sparse hyperspectral unmixing problems. Section IV provides an experimental validation of the considered algorithms using the simulated hyperspectral mixtures from the real and synthetic spectral libraries. The primary reason for the use of the simulated data is that all details of the simulated mixtures are known, and they can be efficiently investigated because they can be manipulated individually and precisely. As a complement to the simulated data experiments, Section V presents an experimental validation of the considered SR and convex optimization algorithms using a well-known hyperspectral scene collected by the AVIRIS instrument over the Cuprite mining district in NV. The USGS spectral library is used in conducting extensive semisupervised unmixing experiments on this scene. Finally, Section VI concludes with some remarks and hints at plausible future research. The Appendix is devoted to the description of the parameter settings used in our experiments and to the strategies followed to infer these parameters.

## II. Spectral Unmixing Reformulated as an SR Problem

In this section, we revisit the classic linear spectral unmixing problem and reformulate it as a semisupervised approach using SR terminology. Furthermore, we review the SR optimization problems that are relevant to our unmixing problem, their theoretical characterization, their computational complexity, and the algorithms that are used to solve them exactly or approximately.

Let us assume that the spectral endmembers that are used to solve the mixture problem are no longer extracted nor generated using the original hyperspectral data as input but are, instead, selected from a library containing a large number of spectral samples available *a priori*. In this case, unmixing amounts to finding the optimal subset of samples in the library that can best model each mixed pixel in the scene. This means that a searching operation must be conducted in a (potentially very large) library, which we denote by $\mathbf{A} \in \mathbb{R}^{L \times m}$, where $L$ and $m$ are the number of spectral bands and the number of materials in the library, respectively. All libraries herein considered correspond to underdetermined systems, i.e., $L < m$. With the aforementioned assumptions in mind, let $\mathbf{x} \in \mathbb{R}^m$ denote the fractional abundance vector with regard to the library $\mathbf{A}$. As usual, we say that $\mathbf{x}$ is a $k$-sparse vector if it has, at most, $k$ components different from zero. With these definitions in place, we can now write our SR problem as

$$\min_{\mathbf{x}} \|\mathbf{x}\|_0 \quad \text{subject to} \quad \|\mathbf{y}-\mathbf{A}\mathbf{x}\|_2 \leq \delta, \quad \mathbf{x} \geq \mathbf{0}, \quad \mathbf{1}^T\mathbf{x}=1 \tag{5}$$

where $\|\mathbf{x}\|_0$ denotes the number of nonzero components of $\mathbf{x}$ and $\delta \geq 0$ is the error tolerance due to the noise and modeling errors. The solution of problem (5), if any, belongs to the set of sparsest signals belonging to the $(m-1)$-probability simplex satisfying error tolerance inequality $\|\mathbf{y}-\mathbf{A}\mathbf{x}\|_2 \leq \delta$. Prior to addressing problem (5), we consider a series of simpler related problems.

### A. Exact Solutions

Let us first start by assuming that the noise is zero and the ANC and ASC constraints are not enforced. Our SR optimization problem is then

$$(P_0): \quad \min_{\mathbf{x}} \|\mathbf{x}\|_0 \quad \text{subject to} \quad \mathbf{A}\mathbf{x} = \mathbf{y}. \tag{6}$$

If the system of linear equations $\mathbf{A}\mathbf{x} = \mathbf{y}$ has a solution satisfying $2\|\mathbf{x}\|_0 < \text{spark}(\mathbf{A})$, where $\text{spark}(\mathbf{A}) \leq \text{rank}(\mathbf{A}) + 1$ is the smallest number of linearly dependent columns of $\mathbf{A}$, it is necessarily the unique solution of $(P_0)$ [30], [31]. The spark of a matrix gives us a very simple way to check the uniqueness of a solution of the system $\mathbf{A}\mathbf{x} = \mathbf{y}$. For example, if the elements of $\mathbf{A}$ are independent and identically distributed (i.i.d.), then with a probability of one, we have $\text{spark}(\mathbf{A}) = m + 1$, implying that every solution with no more than $L/2$ entries is unique.

In our SR problem, we would like then to compute the spark of the hyperspectral library being used to have an idea of what is the minimum level of sparsity of the fractional abundance vectors that can be uniquely determined by solving $(P_0)$. Computing the spark of a general matrix is, however, a hard problem, at least as difficult as solving $(P_0)$. This complexity has fostered the introduction of entities that are simpler to compute, although providing less tight bounds. *Mutual coherence* is such an example. Denoting the $k$th column in $\mathbf{A}$ by $\mathbf{a}_k$ and the $\ell_2$ norm by $\|\cdot\|_2$, the mutual coherence of $\mathbf{A}$ is given by

$$\mu(\mathbf{A}) \equiv \max_{1 \leq k,j \leq m, k \neq j} \frac{\left|\mathbf{a}_k^T \mathbf{a}_j\right|}{\|\mathbf{a}_k\|_2 \|\mathbf{a}_j\|_2} \tag{7}$$

i.e., by the maximum absolute value of the cosine of the angle between any two columns of $\mathbf{A}$. Mutual coherence supplies us with a lower bound for the spark given by [30]

$$\text{spark}(\mathbf{A}) \geq 1 + \frac{1}{\mu(\mathbf{A})}.$$

Unfortunately, as it will be shown further, the mutual coherence of the hyperspectral libraries is very close to one, leading to useless bounds for the spark. In the following, we illustrate two relaxed strategies for computing $(P_0)$: *pursuit algorithms* and *nonnegative signals*.

*1) Pursuit Algorithms:* The problem $(P_0)$ is NP hard (which means that the problem is combinatorial and very complex to solve) [32], and therefore, there is a little hope in solving it in a straightforward way. Greedy algorithms such as the orthogonal basis pursuit [orthogonal matching pursuit (OMP)] [33] and basis pursuit (BP) [34] are two alternative approaches in computing the sparsest solution. BP replaces the $\ell_0$ norm in $(P_0)$ with the $\ell_1$ norm

$$(P_1): \quad \min_{\mathbf{x}} \|\mathbf{x}\|_1 \quad \text{subject to} \quad \mathbf{A}\mathbf{x} = \mathbf{y}. \tag{8}$$

Contrary to problem $(P_0)$, problem $(P_1)$ is convex, and it can be written as a linear programming (LP) problem and can be solved using LP solvers. What is, perhaps, totally unexpected is that, in given circumstances related to matrix $\mathbf{A}$, problem $(P_1)$ has the same solution as problem $(P_0)$. This result is stated in terms of the restricted isometric constants introduced in [27]. Herein, we use the variant proposed in [35]. Let $\alpha_k$, with $\beta_k \geq 0$, be the tightest constants in the inequalities

$$\alpha_k \|\mathbf{x}\|_2 \leq \|\mathbf{A}\mathbf{x}\|_2 \leq \beta_k \|\mathbf{x}\|_2, \quad \|\mathbf{x}\|_0 \leq k \tag{9}$$

and further define

$$\gamma_{2s} \equiv \frac{\beta_{2s}^2}{\alpha_{2s}^2} \geq 1. \tag{10}$$

Then, under the assumption that $\gamma_{2s} < 4\sqrt{2} - 3 \simeq 2.6569$, every $s$-sparse vector is recovered by solving problem $(P_1)$ [35, Th. 2.1 and Corol. 2.1]. Meanwhile, it has been shown that, in some cases, the OMP algorithm also provides the $(P_0)$ solution in a fashion that is comparable with the BP alternative, with the advantage of being faster and easier to implement [26], [36].

*2) Nonnegative Signals:* We now consider the problem

$$\left(P_0^+\right): \quad \min_{\mathbf{x}} \|\mathbf{x}\|_0 \quad \text{subject to} \quad \mathbf{A}\mathbf{x} = \mathbf{y} \quad \mathbf{x} \geq \mathbf{0} \tag{11}$$

and follow a line of reasoning that is close to that of [25]. The hyperspectral libraries generally contain only the nonnegative components (i.e., reflectances). Thus, by assuming that the zero vector is not in the columns of $\mathbf{A}$, it is always possible to find a vector $\mathbf{h}$ such that

$$\mathbf{h}^T \mathbf{A} = \mathbf{w}^T > 0. \tag{12}$$

Since all of the components of $\mathbf{w}$ are nonnegative, matrix $\mathbf{W}^{-1}$, where $\mathbf{W} \equiv \mathrm{diag}(\mathbf{w})$, is well defined, and it has positive diagonal entries. Defining $\mathbf{z} \equiv \mathbf{W}\mathbf{x}$, $c \equiv \mathbf{h}^T\mathbf{y}$, and $\mathbf{D} \equiv \mathbf{A}\mathbf{W}^{-1}$ and noting that

$$\mathbf{h}^T \mathbf{A}\mathbf{W}^{-1}\mathbf{z} = \mathbf{1}^T\mathbf{z} \tag{13}$$

the problem $(P_0^+)$ is equivalent to

$$\left(P_0^+\right): \quad \min_{\mathbf{x}} \|\mathbf{z}\|_0 \quad \text{subject to} \quad \mathbf{D}\mathbf{z} = \mathbf{y} \quad \mathbf{z} \geq \mathbf{0}, \quad \mathbf{1}^T\mathbf{z} = c. \tag{14}$$

We conclude that, when the original signals are nonnegative and the system matrices comply with property (12), then problem (11) enforces the equality constraint $\mathbf{1}^T\mathbf{z} = c$. This constraint has very strong connections with the ASC constraint which is so popular in hyperspectral applications. The ASC is, however, prone to strong criticisms because, in a real image, there is a strong signature variability [37] that, at the very least, introduces positive scaling factors varying from pixel to pixel in the signatures present in the mixtures. As a result, the signatures are defined up to a scale factor, and thus, the ASC should be replaced with a generalized ASC of the form $\sum_i \xi_i x_i = 1$, in which the weights $\xi_i$ denote the pixel-dependent scale factors. What we conclude from the equivalence between problems (11) and (14) is that the nonnegativity of the sources automatically imposes a generalized ASC. For this reason, we do not explicitly impose the ASC constraint.

Similar to problem $(P_0)$, problem $(P_0^+)$ is NP hard and impossible to exactly solve for a general matrix $\mathbf{A}$. As in Section II-A1, we can consider instead $\ell_1$ relaxation

$$\left(P_1^+\right): \quad \min_{\mathbf{x}} \|\mathbf{z}\|_1 \quad \text{subject to} \quad \mathbf{D}\mathbf{z} = \mathbf{y} \quad \mathbf{z} \geq \mathbf{0}. \tag{15}$$

Here, we have dropped the equality constraint $\mathbf{1}^T z = c$ because it is satisfied by any solution of $\mathbf{D}\mathbf{z} = \mathbf{y}$. As with problem $(P_0)$, the condition $\gamma_{2s} < 4\sqrt{2} - 3 \simeq 2.6569$ referred to in Section II-A1 is now applied to the restricted isometric constants of matrix $\mathbf{D}$ to ensure that any $s$-sparse vector solution of $(P_0^+)$ is recovered by solving the problem $(P_1^+)$.

Another way of characterizing the uniqueness of the solution of problem $(P_0^+)$ is *via* the *one-sided coherence* introduced in [25]. However, similar to mutual coherence, the one-sided coherence of the hyperspectral libraries is very close to one, leading to useless bounds. The coherence may be increased by left multiplying the system $\mathbf{D}\mathbf{z} = \mathbf{y}$ with a suitable invertible matrix $\mathbf{P}$[25]. This preconditioning tends to improve the performance of greedy algorithms such as OMP. It leads, however, to an optimization problem that is equivalent to $(P_1^+)$. Thus, a BP solver yields the same solution.

### B. Approximate Solutions

We now assume that the perturbation $\mathbf{n}$ in the observation model is not zero, and we still want to find an approximate solution for our SR problem. The computation of the approximate solutions raises issues that are parallel to those found for exact solutions as addressed earlier. Therefore, we go very briefly through the same topics. Again, we start by assuming that the noise is zero and the ANC and ASC constraints are not enforced. Our noise-tolerant SR optimization problem is then

$$\left(P_0^\delta\right): \quad \min_{\mathbf{x}} \|\mathbf{x}\|_0 \quad \text{subject to} \quad \|\mathbf{A}\mathbf{x} - \mathbf{y}\|_2 \leq \delta. \tag{16}$$

The concept of uniqueness of the sparsest solution is now replaced with the concept of stability [35], [38], [39]. For example, in [38], it is shown that, given a sparse vector $\mathbf{x}_0$ satisfying the sparsity constraint $\mathbf{x}_0 < (1 + 1/\mu(\mathbf{A}))/2$ such that $\|\mathbf{A}\mathbf{x}_0 - \mathbf{y}\| \leq \delta$, then every solution $\mathbf{x}_0^\delta$ of problem $(P_0^\delta)$ satisfies

$$\left\|\mathbf{x}_0^\delta - \mathbf{x}_0\right\|^2 \leq \frac{4\delta^2}{1 - \mu(\mathbf{A})(2\mathbf{x}_0 - 1)}. \tag{17}$$

Notice that, when $\delta = 0$, i.e., when the solutions are exact, this result parallels those ensuring the uniqueness of the sparsest solution. Again, we illustrate two relaxed strategies for computing $(P_0)$.

*1) Pursuit Algorithms:* Problem $(P_0^\delta)$, as $(P_0)$, is NP hard. We consider here two approaches to tackle this problem. The first approach is the greedy OMP algorithm with stopping rule $\|\mathbf{A}\mathbf{x} - \mathbf{y}\|_2 \leq \delta$. The second one consists of relaxing the $\ell_0$

norm to the $\ell_1$ norm, thus obtaining the so-called *BP denoising* (BPDN) optimization problem [34]

$$\left(P_1^{\delta}\right): \quad \min_{\mathbf{x}} \|\mathbf{x}\|_1 \quad \text{subject to} \quad \|\mathbf{A}\mathbf{x}-\mathbf{y}\|_2 \leq \delta. \tag{18}$$

Contrary to problem $(P_0^{\delta})$, problem $(P_1^{\delta})$ is convex, and thus, it is very likely to be solved efficiently with convex optimization methods. As in $(P_0^{\delta})$, the stability of the solution of problem $(P_1^{\delta})$ has also been provided [28], [35]. For example, in [35, Th. 3.1], if $\gamma_{2s} < 4\sqrt{2}-3 \simeq 2.6569$, the $\ell_2$ error between any $s$-sparse solution $\mathbf{x}$ of $\mathbf{A}\mathbf{x}=\mathbf{y}$ and any solution $\mathbf{x}_1^{\delta}$ of $(P_1^{\delta})$ satisfies

$$\left\|\mathbf{x}_1^{\delta}-\mathbf{x}\right\|_2 \leq C\delta \tag{19}$$

where $\delta$ is a constant that depends on the restricted isometric constants $\alpha_{2s}$ and $\beta_{2s}$ defined in (9).

*2) Nonnegative Signals:* We now consider the problem

$$\left(P_0^{\delta+}\right): \quad \min_{\mathbf{x}} \|\mathbf{x}\|_0 \quad \text{subject to} \quad \|\mathbf{A}\mathbf{x}-\mathbf{y}\|_2 \leq \delta, \quad \mathbf{x} \geq 0. \tag{20}$$

Following the reasoning already put forward in Section II-A2, problem $(P_0^{\delta+})$ is equivalent to

$$\min_{\mathbf{z}} \|\mathbf{z}\|_0 \quad \text{subject to} \quad \|\mathbf{D}\mathbf{z}-\mathbf{y}\|_2 \leq \delta, \quad \mathbf{z} \geq 0 \tag{21}$$

where, as in Section II-B2, $\mathbf{D} \equiv \mathbf{A}\mathbf{W}^{-1}$, $\mathbf{W} \equiv \operatorname{diag}(\mathbf{h}^T\mathbf{A})$, and $\mathbf{h}$ is chosen such that $\mathbf{h}^T\mathbf{A} > 0$. From the observation equation $\mathbf{y}=\mathbf{D}\mathbf{z}+\mathbf{n}$ and from $\|\mathbf{n}\| \leq \delta$, we may now write $\mathbf{1}^T\mathbf{z} = c + \mathbf{h}^T\mathbf{n}$, where $c \equiv \mathbf{h}^T\mathbf{y}$. Therefore, the positivity constraint in problem $(P_0^{\delta+})$ together with the property $\mathbf{h}^T\mathbf{A} > 0$ implicitly imposes a soft constraint $\|\mathbf{1}^T\mathbf{z}-c\|_2 \leq \delta_h$, where $\delta_h$ is such that $\|\mathbf{h}^T\mathbf{n}\|_2 \leq \delta_h$.

Similar to $(P_0^{\delta})$, problem $(P_0^{\delta+})$ is NP hard and impossible to solve exactly for a general matrix $\mathbf{A}$ or $\mathbf{D}$. As in Section II-B1, we consider instead the $\ell_1$ relaxation

$$\left(P_1^{\delta+}\right): \quad \min_{\mathbf{z}} \|\mathbf{z}\|_1 \quad \text{subject to} \quad \|\mathbf{D}\mathbf{z}-\mathbf{y}\|_2 \leq \delta \quad \mathbf{z} \geq \mathbf{0}. \tag{22}$$

As with problem $(P_1^{\delta})$, the condition $\gamma_{2s} < 4\sqrt{2}-3 \simeq 2.6569$ is now applied to the restricted isometric constants of matrix $\mathbf{D}$, thus ensuring the stability of the solutions of $(P_1^{\delta+})$.

## III. Algorithms

In the previous section, we have listed a series of optimization problems aimed at computing sparse exact and approximate solutions for our hyperspectral SR problem. In this section, we explain in detail the algorithms that we are going to use for experimental validation in the next two sections. Specifically, we considered five unmixing algorithms, of which three do not explicitly enforce the sparseness of the solution, while the other two belong to the sparse unmixing class of algorithms.

### A. OMP Algorithms

Many variants of the OMP have been published (see [25] and the references therein). Here, we use the standard implementation shown for one pixel in Algorithm 1. The algorithms keeps track of the residual $\mathbf{y}-\mathbf{A}\mathbf{x}^i$, where $\mathbf{x}^i$ is the estimate of $\mathbf{x}$ at the $i$th algorithm iteration. At the first iteration, the initial residual is equal to the observed spectrum of the pixel, the vector of fractional abundances is null, and the matrix of the indices of the selected endmembers is empty. Then, at each iteration, the algorithm finds the member of $\mathbf{A}$ which is best correlated to the actual residual, adds this member to the matrix of endmembers, updates the residual, and computes the estimate of $\mathbf{x}$ using the selected endmembers. The algorithm stops when a stop criterion is satisfied (in our case, when the actual residual is smaller than a preset threshold $T$). A member from $\mathbf{A}$ cannot be selected more than once as the residual is orthogonalized with respect to the members already selected.

---

**Algorithm 1** Pseudocode of the classic OMP algorithm.
**Initialization**:
Iteration: $i = 0$
Initial solution: $\mathbf{x}^0 = \mathbf{0}$
Initial residual: $\mathbf{r}^0 = \mathbf{y}$
Initial matrix of selected indices: $\mathbf{\Lambda}^0 = \mathbf{\Phi}$ (*empty*)
**Main iteration**:
Update iteration: $i \leftarrow i+1$
Compute the index of the best correlated member of $\mathbf{A}$ to the actual residual:
$index \leftarrow \arg\min_{1\leq k\leq m} \|\mathbf{A}_k\mathbf{x}^{i-1} - \mathbf{r}^{i-1}\|_2^2$ where $\mathbf{A}_k$ represents the $k$th column of $\mathbf{A}$
Update support: $\mathbf{\Lambda}^i \leftarrow \mathbf{\Lambda}^{i-1} \cup \{index\}$
Update solution: $\mathbf{x}^i \leftarrow \arg\min_{\mathbf{x}} \|\mathbf{A}_{\Lambda^i}\mathbf{x}-\mathbf{y}\|_2^2$ subject to: Support$\{\mathbf{x}^i\} = \mathbf{\Lambda}^i$
(where $\mathbf{A}_{\Lambda^i}$ is the matrix containing the columns of $\mathbf{A}$ having the indexes from $\mathbf{\Lambda}^i$)
Update residual: $\mathbf{r}^i \leftarrow \mathbf{y}-\mathbf{A}\mathbf{x}^i$
Stop if termination rule: $\|\mathbf{r}^i\|_2^2 \leq T$ is satisfied (the norm of the residual is below a preset threshold $T$)
Otherwise, repeat from **Main iteration**.

---

The OMP may be used in any of the problems listed in Section II. We consider, however, the OMP variation proposed in [25] tailored to problems $(P_0^{+})$ and $(P_0^{\delta+})$, which we denote by OMP$^+$. In this variation, the *Update solution* step in Algorithm 1 is modified to

$$\mathbf{z}^i = \arg\min_{\mathbf{z}} \|\mathbf{D}\mathbf{z}-\mathbf{y}\| \quad \text{subject to} \quad \text{Support}\{\mathbf{z}^i\} = \mathcal{S}^i \quad \mathbf{z} > 0. \tag{23}$$

The OMP and OMP$^+$ stopping rule is adapted to solve either exact or approximate problems. Considering that $\varepsilon$ represents a measure of the error in the accuracy of the unmixing result, in the former case, $\varepsilon$ is very small ($\varepsilon \to 0$), leading to the use of a small $T$ as stopping threshold, whereas in the latter case, $\varepsilon > 0$, which translates to setting a higher value for the stopping threshold $T$ in Algorithm 1.

### B. BP and BPDN Algorithms

In this paper, we also use the recently introduced constrained sparse unmixing algorithm via variable splitting and augmented Lagrangian (CSUnSAL) [29] to solve the linear problems $(P_1)$ and $(P_1^+)$ and the quadratic problems $(P_1^\delta)$ and $(P_1^{\delta+})$. CSUnSAL is tailored to hyperspectral applications with hundreds of thousands or millions of spectral vectors to unmix. This algorithm exploits the alternating direction method of multipliers (ADMM) [40] in a way that is similar to recent works [41], [42]. Here, we use the acronyms CSUnSAL, CSUnSAL$^+$, CSUnSAL$^\delta$, and CSUnSAL$^{\delta+}$ to denote the variant of CSUnSAL tailored to $(P_1)$, $(P_1^+)$, $(P_1^\delta)$, and $(P_1^{\delta+})$ problems, respectively.

### C. Unconstrained BP and BPDN Algorithms

All of the constrained optimization problems $(P_1)$, $(P_1^+)$, $(P_1^\delta)$, and $(P_1^{\delta+})$ can be converted into unconstrained versions by minimizing the respective Lagrangian. For example, the problem $(P_1^\delta)$ is equivalent to

$$\min_{\mathbf{x}} \frac{1}{2}\|\mathbf{Ax}-\mathbf{y}\|_2^2 + \lambda\|\mathbf{x}\|_1. \tag{24}$$

The parameter $\lambda > 0$ is the Lagrange multiplier, and $\lambda \to 0$ when $\delta \to 0$. This model, sometimes referred to as the least squares (LS) $\ell_1$ model, is widely used in the signal processing community. It was used before to address the unmixing problem in [43], in which the endmembers were first extracted from the original image using the N-FINDR endmember extraction algorithm [12], and then, the respective fractional abundances of the endmembers were inferred. However, the N-FINDR algorithm assumes the presence of pure pixels in the original image. To the best of our knowledge, this approach was never used before to address the hyperspectral unmixing problem using spectral libraries.

In this paper, we use the sparse unmixing algorithm via variable splitting and augmented Lagrangian (SUnSAL), introduced in [29], to solve problem (24). SUnSAL, as CSUnSAL, exploits the ADMM method [40] in a way that is similar to [41] and [42]. SUnSAL solves the unconstrained versions of $(P_1)$, $(P_1^+)$, $(P_1^\delta)$, and $(P_1^{\delta+})$. Hereinafter, we use the acronyms SUnSAL, SUnSAL$^+$, SUnSAL$^\delta$, and SUnSAL$^{\delta+}$ to denote the respective variant.

It is important to emphasize that, by setting $\lambda = 0$ in (24), one can arrive to an LS solution of the system, which is obtained by solving the unconstrained optimization problem

$$(P^{\mathrm{LS}}): \quad \min_{\mathbf{x}} \|\mathbf{y}-\mathbf{Ax}\|_2. \tag{25}$$

The solution of optimization problem (25) has a poor behavior in terms of accuracy when the matrix of coefficients is ill conditioned (as it is always the case in the sparse unmixing problem, in which we deal with fat matrices) or when the observations are affected by noise. However, one can take advantage of the physical constraints usually imposed in the unmixing problem (ANC and ASC) by plugging them into the objective function of $(P^{\mathrm{LS}})$. Using this approach, we can simply arrive to the so-called nonnegative constrained LS (NCLS) and fully constrained LS (FCLS) solutions in [7] by first activating the ANC and, then, by activating both the ANC and ASC constraints, respectively. In this paper, we use SUnSAL to solve the constrained versions of the LS problem because, as mentioned before, they are particular cases of (24) when $\lambda = 0$.

### D. ISMA

In this paper, we also use the iterative spectral mixture analysis (ISMA) algorithm [44] to solve the considered problems. The pseudocode of the ISMA is shown in Algorithm 2. The ISMA is an iterative technique derived from the standard spectral mixture analysis formulation presented in (2). It finds an optimal endmember set by examining the change in the root-mean-square error (rmse) after reconstructing the original scene using the fractional abundance estimations, as shown in Algorithm 2. The algorithm consists of two parts. In the first one, the ISMA initially computes an unconstrained solution of the unmixing problem in (2) using all of the spectral signatures available in a spectral library $\mathbf{A}$. Then, it removes the signature with the lowest estimated fractional abundance in $\mathbf{x}^i$ and repeats the process with the remaining signatures until only one signature remains. In the second part of the algorithm, the so-called critical iteration is identified as the iteration corresponding to the first abrupt change in the rmse, computed as follows:

$$\Delta\mathrm{rmse} \equiv 1 - \left(\frac{\mathrm{rmse}_{j-1}}{\mathrm{rmse}_j}\right) \tag{26}$$

where $\mathrm{rmse}_j$ is the rmse corresponding to the $j$th iteration. The critical iteration corresponds to the optimal set of endmembers. The idea of recovering the true endmember set by analyzing the change in the rmse is based on the fact that, before finding the optimal set of endmembers, the rmse varies in certain (small) limits, and it has a bigger variation when one endmember from the optimal set is removed, as the remaining endmembers are not sufficient to model with good accuracy the actual observation. It is important to emphasize that the ISMA computes, at each iteration, an unconstrained solution instead of a constrained one. This is because it is predictable that, when the set of endmembers approaches the optimal one, the estimated fractional abundance vector $\widehat{\mathbf{x}}$ will actually approach $\mathbf{x}$, which is the true one.

---

**Algorithm 2** Pseudocode of the ISMA algorithm.

**Part 1**:

**Initialization**:

Iteration: $i = 1$

Initial spectral library: $\mathbf{A^1} \leftarrow \mathbf{A}$

**Main iteration**:

Compute solution: $\mathbf{x}^i \leftarrow \arg\min_x \|\mathbf{A^i x} - \mathbf{y}\|_2^2$

Compute $\mathrm{rmse}^i \leftarrow (1/\sqrt{L})\|\widehat{\mathbf{y}} - \mathbf{y}\|_2$, where $\widehat{\mathbf{y}} = \mathbf{A}^i\mathbf{x}^i$

Compute the member of $\mathbf{A}^i$ having the lowest abundance: $index \leftarrow \min_k(\mathbf{x_i^k})$

Remove the member having the lowest fractional abundance from the spectral library: $\mathbf{A^i} \leftarrow \mathbf{A^i} \backslash \mathbf{A^i_{index}}$

If $\mathbf{A}$ still contains more than one member, update iteration: $i \leftarrow i+1$ and repeat **Main iteration**

**Part 2**:

Compute the variation of the rmse for all iterations $i_{\min} \leq i \leq m : \Delta\text{rmse}_i = 1 - \text{rmse}_{i-1}/\text{rmse}_i$ (where $i_{\min}$ is the minimum number of iterations before stopping the search)

Determine the position of the first substantial increase in $\Delta$rmse (*the critical iteration*): $i_{\Delta\text{rmse}_{\max}}$

The final solution is the solution computed in **Part 1** at the critical iteration.

## IV. Experiments With Simulated Data

In this section, we run a series of simulated data experiments which are mainly intended to address two fundamental questions.

1) What is the minimum sparsity of signals which are recoverable using the hyperspectral libraries?
2) Among the optimization problems and respective algorithms, what are the more suitable ones to address the hyperspectral SR problem?

This section is organized as follows. First, we describe the spectral libraries used in our simulated data experiments and the performance discriminators. Then, we compute the approximate solutions without imposing the ASC (due to the reasoning showed in Section II-A2) for simulated mixtures using the techniques described in Section III. We do not address the unmixing problem when the observations are not affected by noise since, in this case and for the levels of sparsity considered, all of the methods were able to recover the correct solution. Furthermore, we present a comparison of the algorithms used to solve the unmixing problem from two viewpoints: their computational complexity and their behavior with different noise levels. Next, a short example is dedicated to the case when the ASC holds (for one particular library and with observations affected by correlated noise). The last experiment of this section exemplifies the application of sparse unmixing techniques to spectral libraries composed of image-derived endmembers, which is an approach that can be adopted if no spectral library is available *a priori*. This section concludes with a summary of the most important aspects observed in our simulated data experiments.

### A. Spectral Libraries Used in the Simulated Data Experiments

We have considered the following spectral libraries in our experiments.

1) $\mathbf{A}_1 \in \mathbb{R}^{224\times 498}$: A selection of 498 materials (different mineral types) from the USGS library denoted as splib06[3] and released in September 2007. The reflectance values are measured for 224 spectral bands distributed uniformly in the interval 0.4–2.5 $\mu$m.
2) $\mathbf{A}_2 \in \mathbb{R}^{224\times 342}$: Subset of $\mathbf{A}_1$, where the angle between any two different columns is larger than 3°. We have made this pruning because there are many signatures in $\mathbf{A}_1$ which correspond to very small variations (including scalings) of the same material.
3) $\mathbf{A}_3 \in \mathbb{R}^{224\times 500}$: A selection of 500 materials generated using a spectral library generator tool, which allows a user to create a spectral library starting from the ASTER library,[4] which is a compilation of over 2400 spectra of natural and man-made materials. Specifically, each of the members has the reflectance values measured for 224 spectral bands distributed uniformly in the interval 3–12 $\mu$m. In this library, there were selected spectra corresponding to materials of the following types: man-made (30), minerals (265), rocks (130), soil (40), water (2), vegetation (2), frost/snow/ice (1), and stony meteorites (30). Notice that, in a real scenario, a library like this is not likely to be used as it is expected that a given mixture does not contain materials of so many different types. Although real hyperspectral images are acquired usually in a narrower range of wavelengths, this library represents an interesting case study since it is highly heterogeneous from the viewpoint of the type of materials that actually compose it, compared to $\mathbf{A}_1$ and $\mathbf{A}_2$ (which contain only the mineral spectra). At the same time, using this library leads to more challenging unmixing problem due to the internal characteristics of the library, as it will be seen further.
4) $\mathbf{A}_4 \in \mathbb{R}^{224\times 449}$: Subset of $\mathbf{A}_3$, generated following the same reasonings as that for $\mathbf{A}_2$.

For comparative purposes, we also consider the following two libraries made of i.i.d components:

5) $\mathbf{A}_5 \in \mathbb{R}^{224\times 440}$: made of i.i.d. Gaussian components having a zero mean and a variance of one;
6) $\mathbf{A}_6 \in \mathbb{R}^{224\times 440}$: made of i.i.d. components uniformly distributed in the interval [0, 1].

Fig. 3(a) shows the mean signature and two other signatures randomly chosen from library $\mathbf{A}_1$. All of the curves shown are nonnegative and relatively smooth. These characteristics are also shown in Fig. 3(b), which shows the mean square value of the Discrete Cosine Transform coefficients computed over all signatures of the library $\mathbf{A}_1$, together with their cumulative energy. From this plot, we can conclude that 99.9% of the energy is contained in the first 21 coefficients. If we assume that (from a practical point of view) the remaining coefficients are zero, then the spark of $\mathbf{A}_1$ should be no larger than 21. This results from the following.

1) Computing the DCT of the columns of $\mathbf{A}$ is equivalent to left multiplying $\mathbf{A}$ by a unitary $L \times L$ matrix, which does not therefore change spark$(\mathbf{A})$.
2) Any matrix with zero elements for any line greater that a given natural $l$ has a rank that is not larger than $l$.

Table I characterizes the libraries $\mathbf{A}_1$–$\mathbf{A}_6$. We draw attention on the very high values of the coherence for the spectral libraries (both original and pruned versions). The upper limits of the spark values for libraries $\mathbf{A}_1$–$\mathbf{A}_4$ anticipate the difficulties

[3] Available online at http://speclab.cr.usgs.gov/spectral.lib06.

[4] Available online at http://speclib.jpl.nasa.gov.

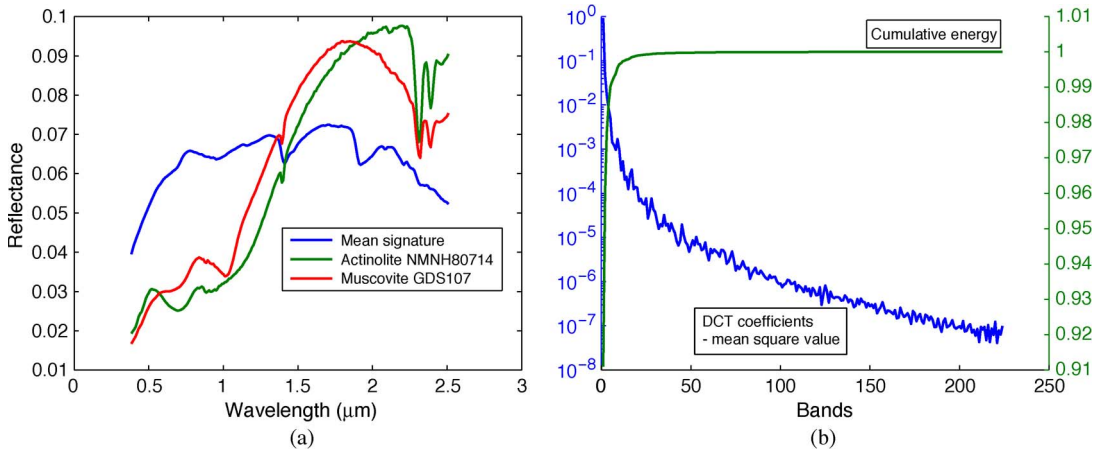


Fig. 3. (a) Mean signature and two other signatures randomly chosen from library $\mathbf{A}_1$. (b) DCT coefficients and cumulative energy.

TABLE I
MUTUAL COHERENCE VALUES AND ESTIMATION OF THE SPARK FOR DIFFERENT SPECTRAL LIBRARIES

| Spectral library | $\mathbf{A}_1$ | $\mathbf{A}_2$ | $\mathbf{A}_3$ | $\mathbf{A}_4$ | $\mathbf{A}_5$ | $\mathbf{A}_6$ |
|---|---|---|---|---|---|---|
| Description | USGS | USGS pruned | ASTER | ASTER pruned | i.i.d. Gaussian | i.i.d. Uniform |
| Number of spectra ($t$) | 498 | 342 | 500 | 449 | 440 | 440 |
| Number of spectral bands ($L$) | 224 | 224 | 224 | 224 | 220 | 220 |
| Minimum wavelength ($w_{min}$) in $\mu$m | 0.4 | 0.4 | 3 | 3 | - | - |
| Maximum wavelength ($w_{max}$) in $\mu$m | 2.5 | 2.5 | 12 | 12 | - | - |
| spark($\mathbf{A}$) (upper bound) | 21 | 23 | 30 | 54 | 221 | 221 |
| Mutual coherence $\mu(S)$ | 0.99998 | 0.9986 | 1 | 0.9986 | 0.3141 | 0.8388 |

in the SR. These difficulties are somehow mitigated by the very low level of sparsity of the signal in which we are interested. On the other hand, it is important to emphasize that libraries composed of i.i.d. components (similar to $\mathbf{A}_5$ and $\mathbf{A}_6$) have been extensively used in the literature in order to investigate the ability of different algorithms to deal with underdetermined systems of equations. In a sparse unmixing context, the use of these libraries is mainly intended to preliminarily validate the algorithms used. This is because these libraries represent ideal situations that are never encountered in real scenarios, as it can be concluded from Table I. In the following sections, we present a series of simulation results based on the aforementioned libraries and aimed at assessing the potential of SR techniques in the context of hyperspectral unmixing applications.

### B. Performance Discriminators

Before presenting our experimental results, first, it is important to describe the parameter settings and performance discrimination metrics adopted in our experiments. Regarding parameter settings, the algorithms described in Section III have been applied to unmix simulated mixtures containing a number of endmembers (i.e., values of the sparsity level), which ranges from 2 to 20. For each considered cardinality, spectral library, and noise level, we generated 100 mixtures containing random members from the library. The fractional abundances were randomly generated following a Dirichlet distribution [14]. The ISMA, OMP, and OMP+ algorithms were constrained to return solutions having at most 30 endmembers (we assume that it is not plausible that a mixed pixel contains more materials). Also, the rmse variation for the ISMA ($\Delta$rmse) was simply related to the difference between two consecutive values of the rmse: $\Delta\text{rmse}_i \equiv \text{rmse}_i - \text{rmse}_{i-1}$. We remind that the ISMA is a per-pixel optimization method. This means that the stopping criterion should be individually set for each pixel separately, which is impossible in real scenes with thousands or tens of thousands of pixels. In our experiments, the stopping criterion was set for a large number of samples at once. The semioptimal parameters that we have empirically set in our experiments are reported in the Appendix (see Table IV for additional details). It is important to emphasize that, in Table IV and in all of the following figures, the algorithms OMP, ISMA, SUnSAL, and CSUnSAL are used to solve the unmixing problems $(P_1)$ and $(P_1^\delta)$, whereas the SUnSAL+ and CSUnSAL+ algorithms are used to solve the problems $(P_1^+)$ and $(P_1^{\delta+})$. Finally, algorithms SUnSAL + D and CSUnSAL + D solve the modified problems shown in (15). SUnSAL also solves the NCLS problem. It is also important to note that algorithms OMP+, SUnSAL + D, and CSUnSAL + D were not applied for library $(\mathbf{A_5})$ as the corresponding technique is dedicated to nonnegative signals.

Regarding the adopted performance discriminators, the quality of the reconstruction of a spectral mixture was measured using the signal-to-reconstruction error $\text{SRE} \equiv E[\|\mathbf{x}\|_2^2]/E[\|\mathbf{x} - \widehat{\mathbf{x}}\|_2^2]$ measured in decibels: $\text{SRE(dB)} \equiv 10\log_{10}(\text{SRE})$. We use this error measure, instead of the classical rmse, as it gives more information regarding the power of the error in relation with the power of the signal. We also computed the so-called "probability of success" $p_s$, which is an estimate of

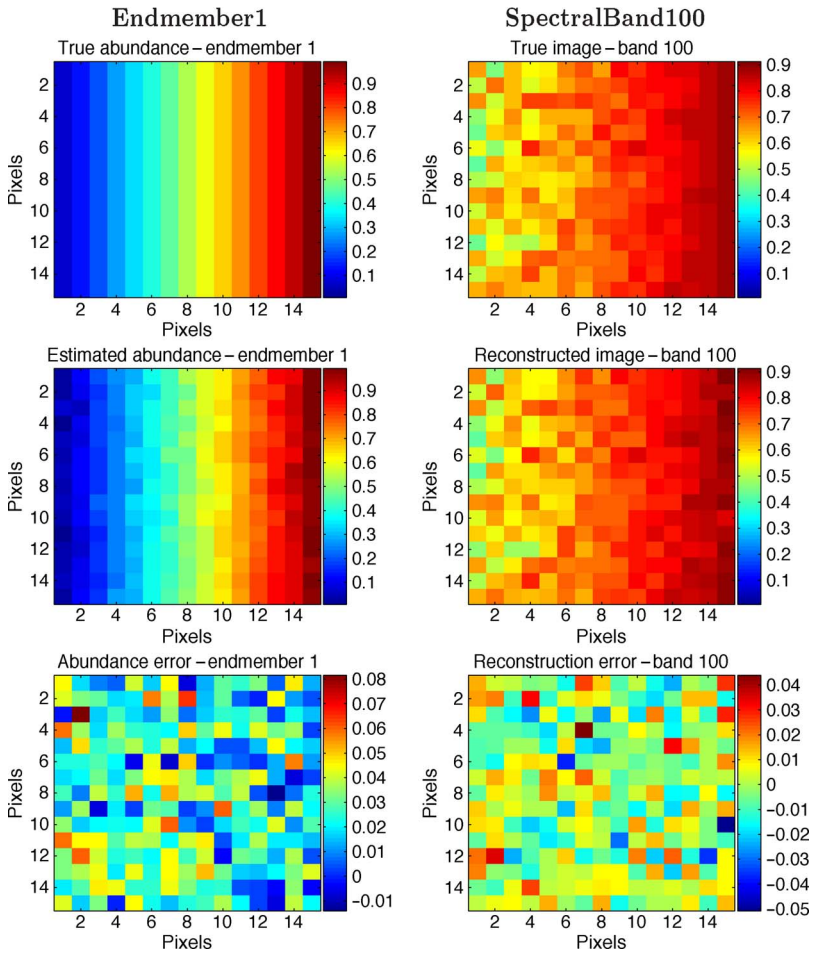


Fig. 4. Toy example illustrating the reconstruction quality obtained for SRE(dB) $\approx 5$ dB. The figures at the top, respectively, represent the abundance fractions of an endmember and the reflectance values of spectral band 100 (1.28 $\mu$m) in the toy hyperspectral image, and the figures in the middle represent the respective estimations using the SUnSAL algorithm, while the figures at the bottom show the corresponding differences between the true and estimated values in both cases.

the probability that the relative error power is smaller than a certain threshold. This metric is a widespread one in SR literature and is formally defined as follows: $p_s \equiv P(\|\widehat{x} - x\|^2/\|x\|^2 \leq threshold)$. For example, if we set $threshold = 10$ and get $p_s = 1$, this means that the total relative error power of the fractional abundances is (with a probability of one) less than 1/10. This gives an indication about the stability of the estimation that is not directly inferable from the SRE (which is an average). In our case, the estimation result is considered successful when $\|\widehat{x} - x\|^2/\|x\|^2 \leq 3.16$ (5 dB). In all of the following figures related to the SRE(dB), we plot a dashed blue line representing the 5-dB level in all situations in which at least one of the algorithms reaches this value. The main rationale for using this threshold is that, after inspecting the results of different unmixing scenarios, we concluded that a reconstruction attaining SRE(dB) $= 5$ dB is still useful. To illustrate this situation, we simulated a toy hyperspectral image with dimensions of $15 \times 15$ pixels using the spectral library $\mathbf{A}_1$. We assumed the presence of five randomly selected endmembers in all simulated pixels, with all observations affected by a white noise with the signal-to-noise ratio (SNR $\equiv \|\mathbf{Ax}\|^2/\|\mathbf{n}\|_2^2$) given as SNR $= 40$ dB. For a better visual perception of the unmixing results, the fractional abundance of one of the endmembers follows a deterministic

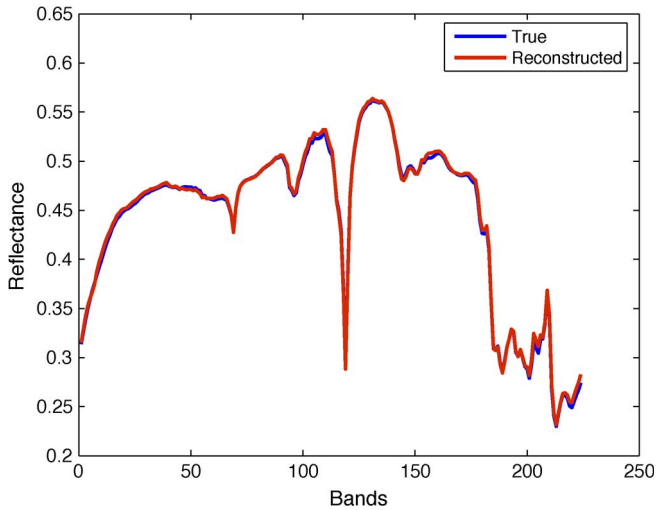


Fig. 5. (Blue) True and (red) reconstructed spectra of a randomly selected pixel in a toy hyperspectral image simulated with SRE(dB) $= 5.2$ dB.

pattern (e.g., a staircase shape with 15 values comprised between 0 and 1), with the other abundances generated randomly (such that the ASC holds in each pixel). Fig. 4 shows the true and inferred abundance maps obtained for the first endmember when SRE(dB) $= 5.3$ dB after applying the SUnSAL algorithm. Fig. 4 also shows the true and reconstructed reflectance

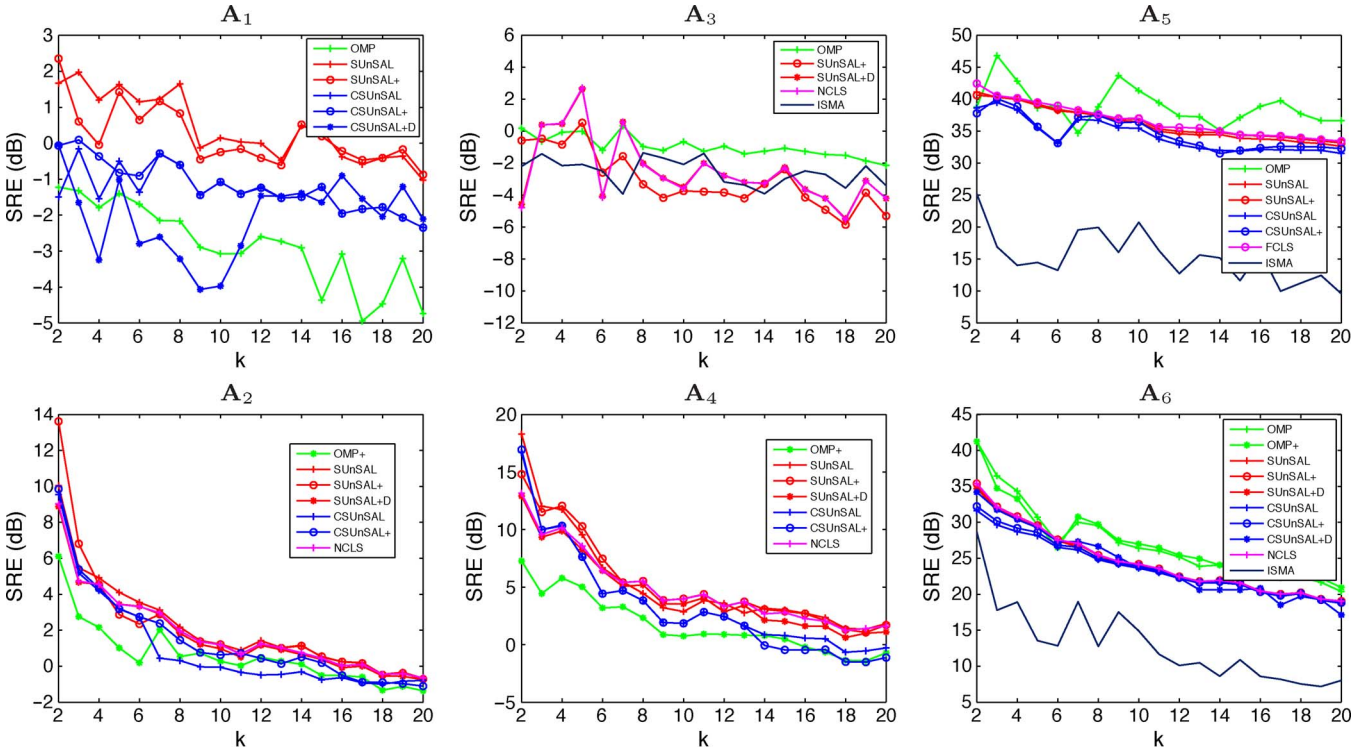


Fig. 6. Plot of the SRE(dB) values (as a function of the number of endmembers) obtained by the different sparse unmixing methods when applied to the simulated data with white noise (SNR = 30 dB) using different spectral libraries.

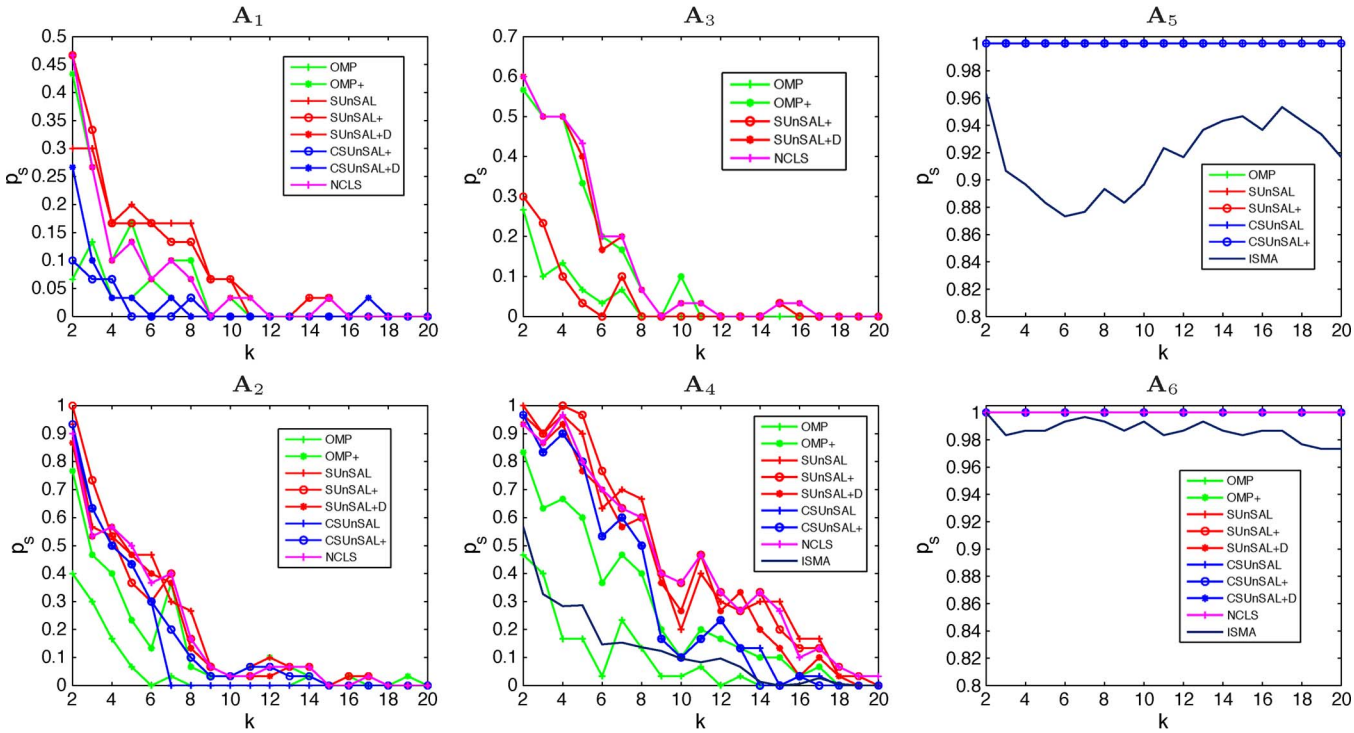


Fig. 7. Plot of the $p_s$ values (as a function of the number of endmembers) obtained by the different sparse unmixing methods when applied to the simulated data with white noise (SNR = 30 dB) using different spectral libraries.

values at spectral band number 100 (1.28 $\mu$m) of our toy hyperspectral image. Finally, the last row of Fig. 4 shows the difference images (which represent the per-pixel differences between the images in the top and middle rows of the same figure) in order to represent the magnitude of the errors that occurred in the estimation of fractional abundances and in the image reconstruction at the considered spectral band. Note the low values of the errors achieved in both cases. The simple toy example in Fig. 4 indicates that a reconstruction with SRE(dB) $\geq$ 5 dB can be considered of good accuracy. Fig. 5 also shows the true and reconstructed spectra of a randomly selected pixel in our toy hyperspectral image. In Fig. 5, the reconstructed spectrum

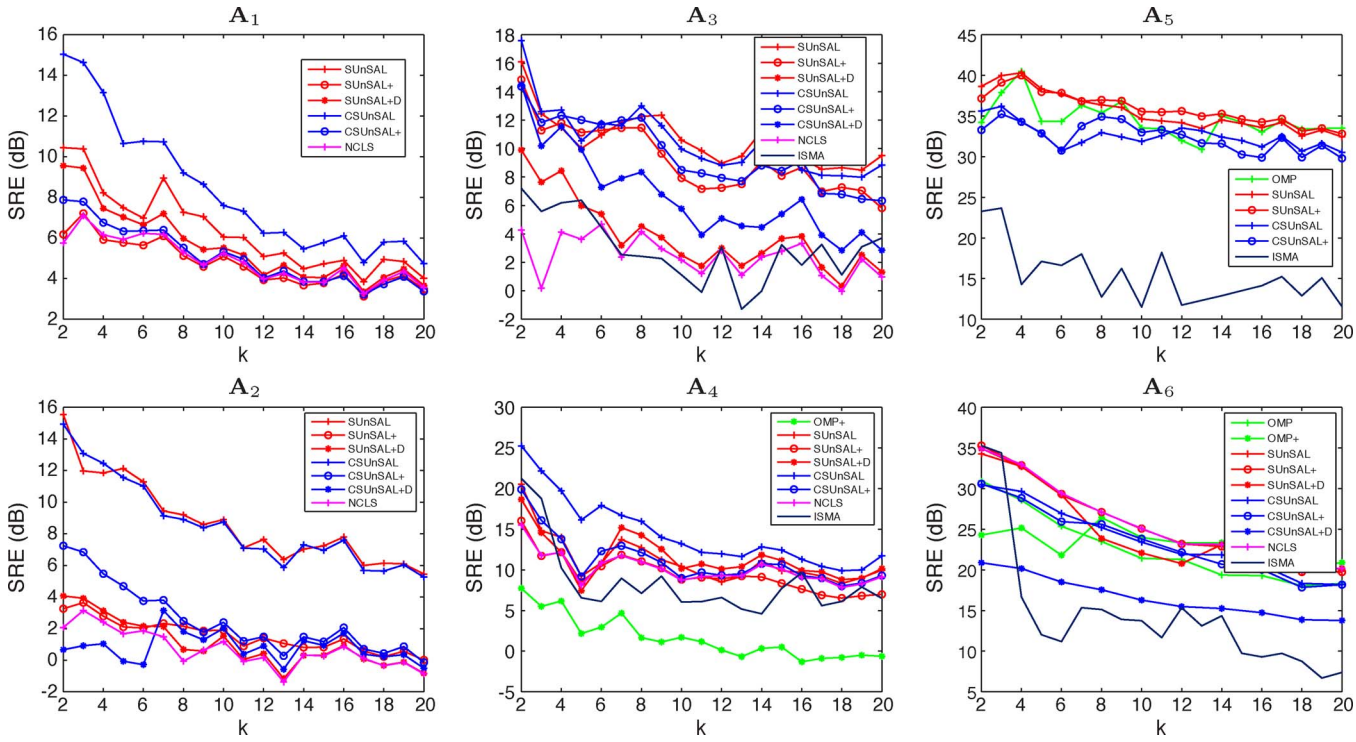


Fig. 8. Plot of the SRE(dB) values (as a function of the number of endmembers) obtained by the different sparse unmixing methods when applied to the simulated data with correlated noise (SNR = 30 dB) using different spectral libraries.

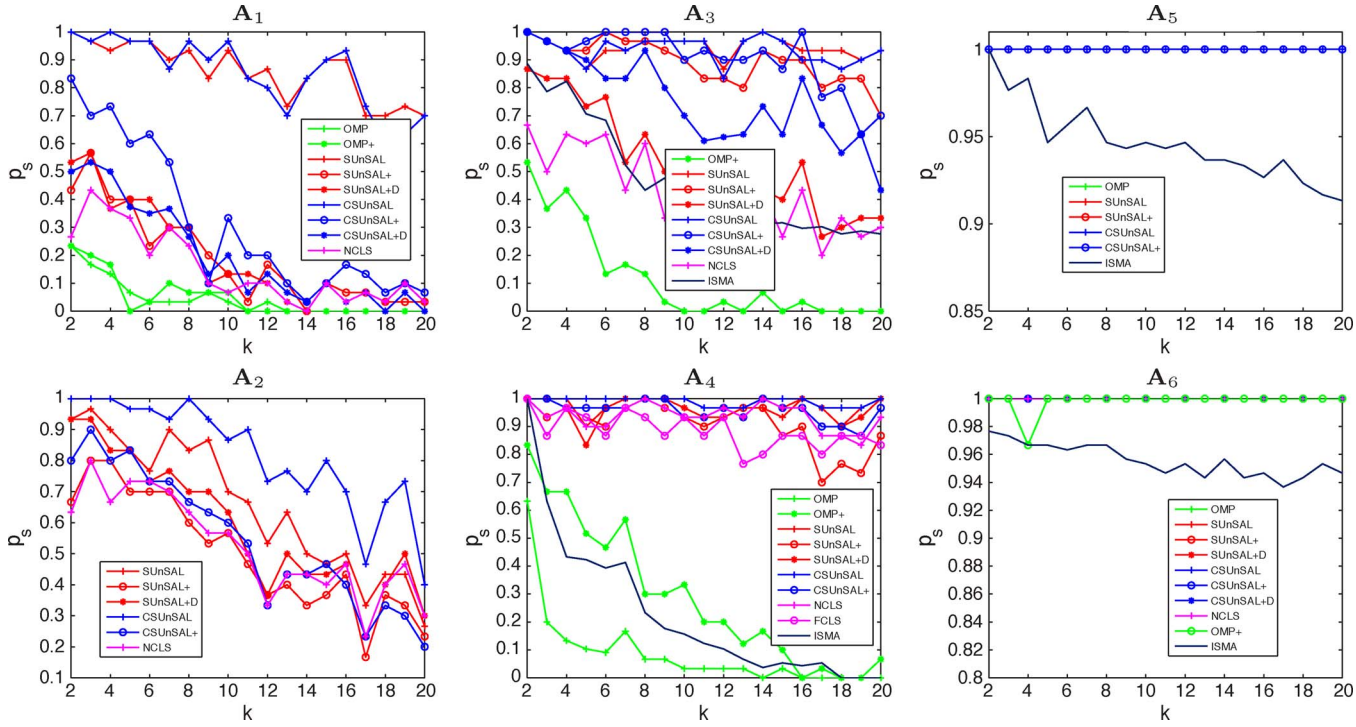


Fig. 9. Plot of the $p_s$ values (as a function of the number of endmembers) obtained by the different sparse unmixing methods when applied to the simulated data with correlated noise (SNR = 30 dB) using different spectral libraries.

was obtained for SRE(dB) = 4.8 dB. Moreover, while, in this example, the noise was set to a low value, in the following tests, the observations are affected by higher noise (SNR = 30 dB), which means that the chosen threshold is even more powerful in terms of performance discrimination.

### *C. Calculation of the Approximate Solutions Without Imposing the ASC Constraint*

In this section, we consider that the observations are affected by noise, i.e., $\mathbf{n} \neq 0$. The SNR was set to 30 dB. This noise level was chosen after analyzing the SNR estimated using the

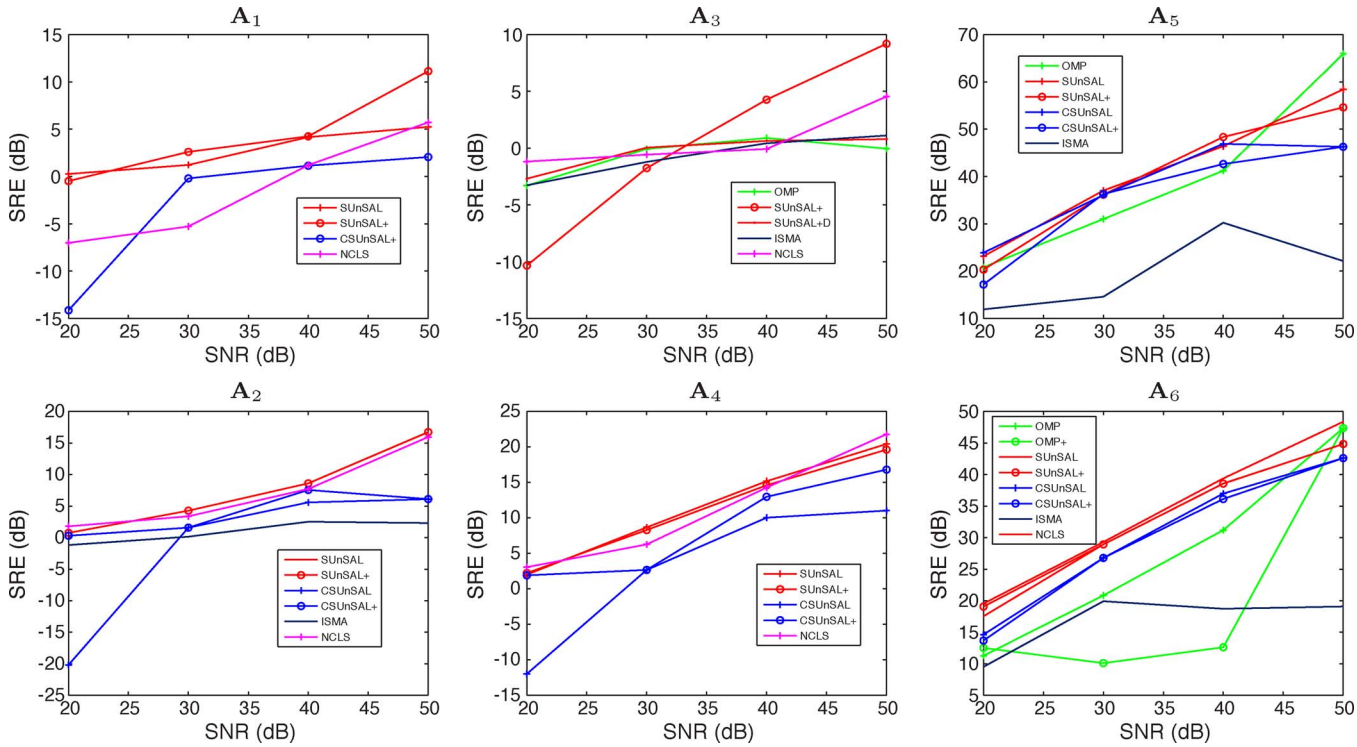


Fig. 10. Plot of the SRE(dB) values (as a function of the considered SNR) obtained by the different sparse unmixing methods when applied to the simulated data with white noise using different spectral libraries.

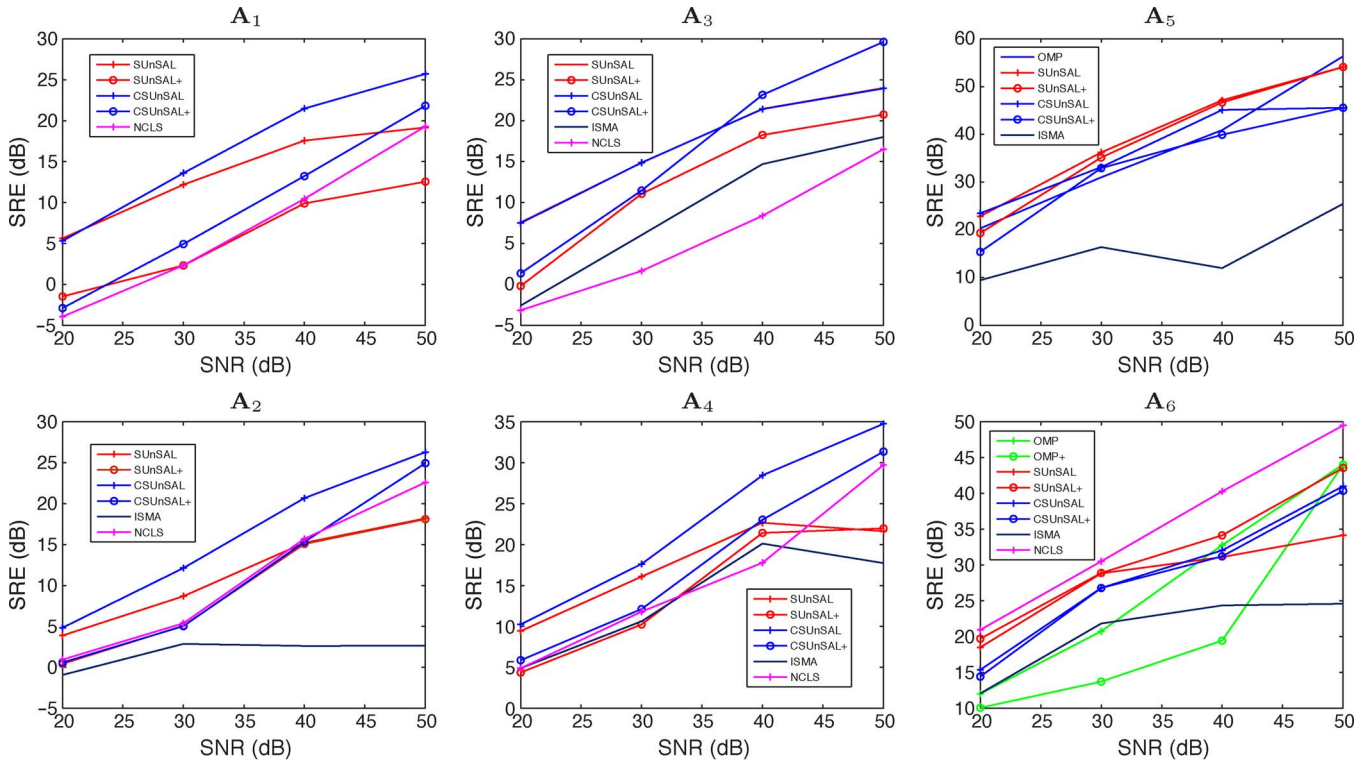


Fig. 11. Plot of the SRE(dB) values (as a function of the considered SNR) obtained by the different sparse unmixing methods when applied to the simulated data with correlated noise using different spectral libraries.

VCA [14] algorithm[5] in several real hyperspectral images and for different values of the number of endmembers assumed to be present in the respective scenes.

[5]Demo available online at http://www.lx.it.pt/ bioucas/code.htm.

It is important to emphasize that the additive perturbation in the model described in (2) may be motivated by several causes, including system noise, Poisson noise related with the photon counting process, and modeling errors related with deviations in the spectral signatures resulting from atmospheric interferers

or nonlinearities in the observation mechanism. The first two causes usually introduce band uncorrelated noise, whereas the latter one yields band correlated noise. In hyperspectral imaging applications, we argue that the correlated noise is a major concern since it is very difficult to calibrate the observations resulting from an airborne/spaceborne sensor with regard to those in a spectral library of signatures that are acquired in a laboratory and that are free of atmospheric interferers, leaving the spectral variability issues alone. Taking into account that, in real applications, the noise is highly correlated as it mainly represents the modeling noise and the spectra are of low-pass type with respect to the wavelength, in our simulations, we considered, on the one hand, the white noise and, on the other hand, the colored noise resulting from low-pass filtering the i.i.d. Gaussian noise using a normalized cutoff frequency of $5\pi/L$. For a given mixture, the unmixing process was again considered successful when SRE(db) $\geq 5$ dB. In the following, we describe our experiments by assuming white and correlated noise, respectively.

*1) Experiments Assuming White Noise:* Fig. 6 shows the SRE(dB) obtained for our simulated observations affected by white noise. Similarly, Fig. 7 shows the probability of success $p_s$ achieved by each method for the simulated observations affected by white noise. It should be noted that we removed the curves corresponding to algorithms with poor behavior from the plots in Figs. 6 and 7. From these figures, we can conclude that pruning the libraries can improve the performances of the algorithms when the observations are affected by white noise. Fig. 7 shows that the highest probability of success is achieved by SUnSAL (specifically, by its positive constrained version) and NCLS. The library $\mathbf{A}_3$ seems to be the most difficult one to treat for all methods (being the most coherent matrix), but its pruned version is much more accessible. CSUnSAL particularly exhibits a significant performance improvement when pruning the libraries. For the libraries composed of real signatures ($\mathbf{A}_1, \ldots, \mathbf{A}_4$), the probability of success is low for all methods when the cardinality is higher than ten. Nevertheless, in a sparse unmixing framework, we are interested in solutions with a smaller number of endmembers, e.g., up to five endmembers per pixel. For the libraries composed of i.i.d. entries, all methods exhibit a good behavior. For the other libraries, the ISMA and OMP exhibit poor results.

*2) Experiments Assuming Correlated Noise:* Fig. 8 shows the SRE(dB) obtained for our simulated observations affected by correlated noise. Similarly, Fig. 9 shows the probability of success $p_s$ obtained for our simulated observations affected by correlated noise. From the viewpoint of our considered problem, perhaps, this is the most interesting case study since the noise in the hyperspectral images is usually correlated. In Figs. 8 and 9, it can be observed that most considered sparse unmixing methods exhibit a better performance when applied to observations affected by colored noise. As in previous (and subsequent) experiments, we removed the curves corresponding to algorithms with poor behavior. For the libraries composed of real signatures, the highest probability of success is achieved by CSUnSAL and/or its variants, closely followed by the unconstrained version of SUnSAL (see the plots for the most difficult cases, corresponding to $\mathbf{A_1}$ and $\mathbf{A_3}$). This result confirms our introspection that imposing sparsity can lead to improved results in the context of hyperspectral unmixing problems using the spectral libraries.

### *D. Comparison of the Unmixing Algorithms With Regard to Computational Complexity*

An important issue in the evaluation of the sparse unmixing algorithms is their computational complexity, particularly when large spectral libraries are used to solve the unmixing problem. In this regard, we emphasize that both OMP (and its variations) and ISMA are computationally complex, with cubic running time O($L^3$). All remaining algorithms (NCLS, FCLS, SUnSAL and its variations, and CSUnSAL and its variations) have the same theoretical complexity, with quadratic running time O($L^2$). A more detailed comparison reporting the actual algorithm running times in the task of unmixing a real hyperspectral scene is given (for the same computing environment) in Section V.

### *E. Comparison of the Unmixing Algorithms in the Presence of Different Noise Levels*

In this section, we compare the performances of the considered sparse unmixing algorithms with different noise levels. Specifically, we consider SNR levels of 20, 30, 40, and 50 dB both for white and correlated noise. In this experiment, the observations were generated by assuming a fixed cardinality of the solution: $\mathrm{k} = 5$. Fig. 10 shows the SRE(dB) as a function of the noise level affecting the measurements in the case of white noise, while Fig. 11 shows the same plots in the case of measurements affected by correlated noise for different spectral libraries. Again, we removed the curves corresponding to algorithms with poor behavior. The algorithm parameters in this experiment were set using the procedure described in the Appendix (see Table V). In Figs. 10 and 11, we can conclude that the performance of the algorithms decreases when the noise increases, as expected. In general, the algorithm behavior observed in previous simulated scenarios is confirmed here, with the general trend that most considered approaches perform better in the presence of correlated noise rather than in the presence of white noise. For the white noise scenario, both SUnSAL and SUnSAL+ generally provide the highest values of SRE(dB), particularly for high SNR values. For the correlated noise scenario, CSUnSAL and its variation CSUnSAL+ generally provide the highest scores of SRE(dB), with the exception of spectral library $\mathbf{A}_6$ for which NCLS provides the highest error scores as it was already the case in previous experiments. To conclude this section, it is worth mentioning that we evaluated the performance of the proposed method not only with different libraries and a fixed cardinality of the solution (as shown in Figs. 10 and 11) but also with a fixed library and a variable cardinality of the solution. For instance, extensive experiments conducted using only the library $\mathbf{A}_1$ for different cardinalities of the solution (not included here for space considerations) led to the same conclusions obtained using all of the libraries.

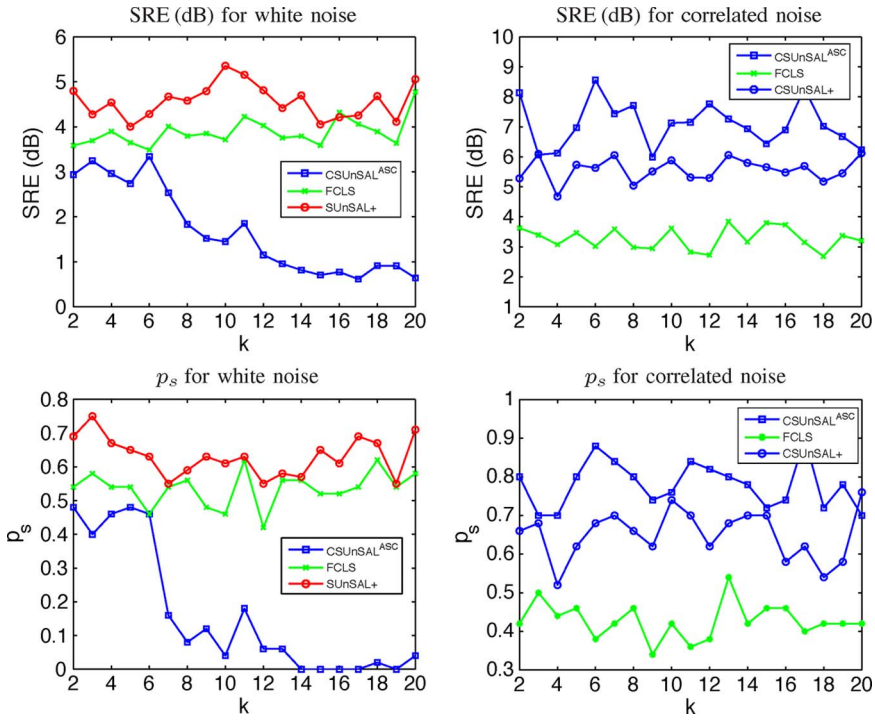


Fig. 12. Plot of the SRE(dB) and $p_s$ values (as a function of the number of endmembers) obtained by the different sparse unmixing methods, including the ASC constraint, when applied to the simulated data with white and correlated noise using spectral library $\mathbf{A}_1$.

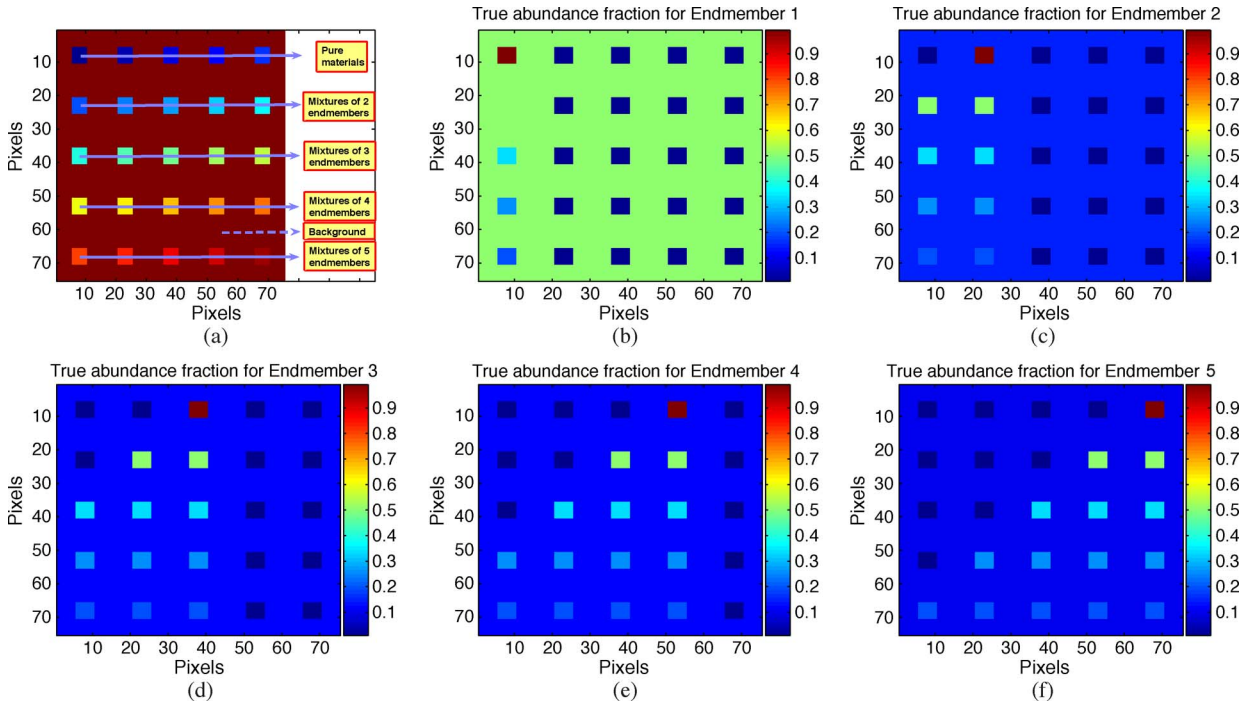


Fig. 13. Simulated data set constructed to evaluate the possibility of applying the sparse unmixing methods using the image-derived endmembers. (a) Simulated image. (b) Abundances of endmember #1. (c) Abundances of endmember #2. (d) Abundances of endmember #3. (e) Abundances of endmember #4. (f) Abundances of endmember #5.

### *F. Calculation of the Approximate Solutions Imposing the ASC Constraint*

This section discusses the results obtained in a noisy environment by the techniques presented in Section III, which include the ASC constraint, denoted by SUnSAL$^{\mathrm{ASC}}$ (which also solves here the FCLS problem) and CSUnSAL$^{\mathrm{ASC}}$. The simulated data were generated as explained in Section IV-C but imposing this time the ASC constraint and adding both white and correlated noise to the simulated observations. The spectral library used in this example is $\mathbf{A}_1$. When the ASC holds, SUnSAL$^{\mathrm{ASC}}$ is equal to FCLS since, no matter how the parameter $\lambda$ is chosen, the sparsity enforcing term does

TABLE II
SRE(dB) VALUES ACHIEVED AFTER APPLYING SUnSAL+ TO THE IMAGE-DERIVED ENDMEMBERS FROM THE SIMULATED IMAGE IN FIG. 13

| | Results for different values of $\lambda$ | | | | |
|---|---|---|---|---|---|
| | $\lambda = 10^{-1}$ | $\lambda = 5 \times 10^{-2}$ | $\lambda = 10^{-3}$ | $\lambda = 5 \times 10^{-4}$ | NCLS: $\lambda = 0$ |
| Mean SRE (dB) | 9.60 | 10.82 | 12.09 | 12.62 | 9.10 |
| | Results for different endmembers | | | | |
| | endmember #1 | endmember #2 | endmember #3 | endmember #4 | endmember #5 |
| Mean SRE (dB) | 22.82 | 1.33 | 10.91 | 13.75 | 5.42 |

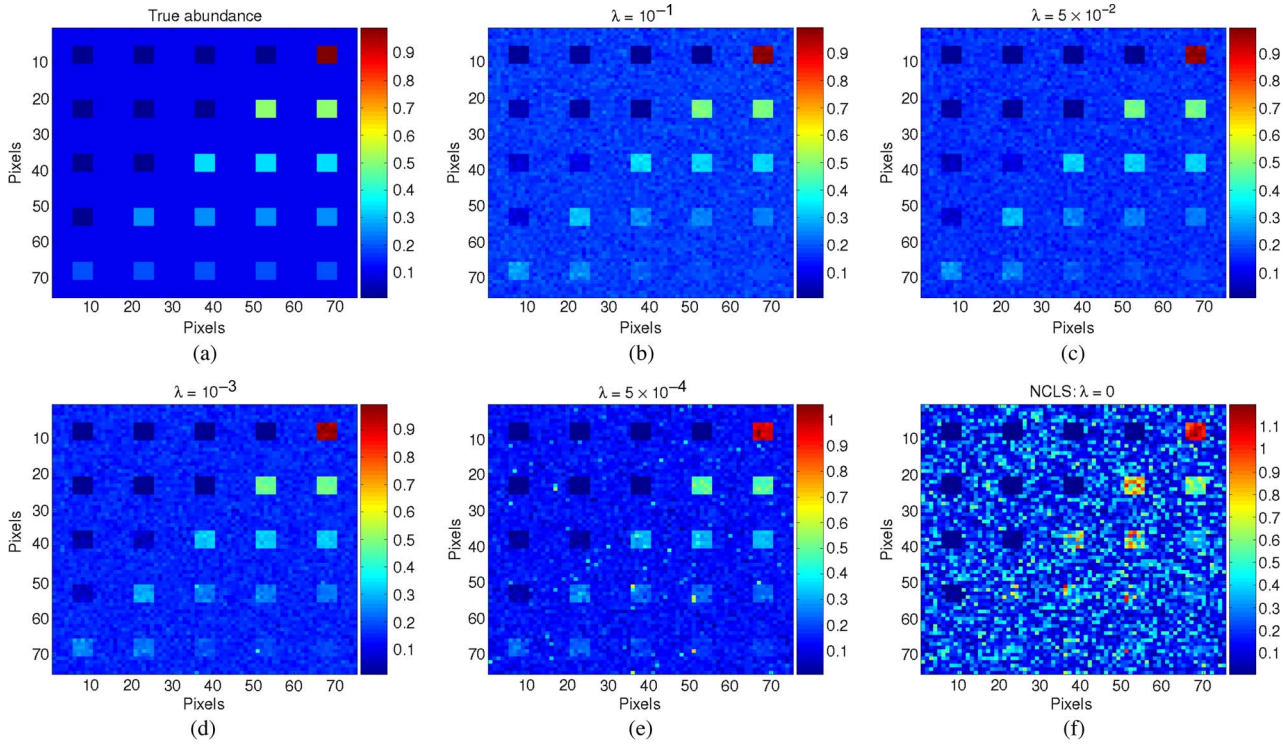


Fig. 14. True and estimated abundance fractions for one of the simulated endmembers (all results were obtained using SUnSAL+ for different values of the parameter $\lambda$). (a) True abundances for endmember #5. (b) Estimations with $\lambda = 10^{-1}$ and SRE(dB) $= 5.43$. (c) Estimations with $\lambda = 5 \times 10^{-2}$ and SRE(dB) $= 6.85$. (d) Estimations with $\lambda = 10^{-3}$ and SRE(dB) $= 8.41$. (e) Estimations with $\lambda = 5 \times 10^{-4}$ and SRE(dB) $= 8.22$. (f) Estimations with $\lambda = 0$ and SRE(dB) $= -1.82$.

not play any role (it is a constant). As a consequence, we do not plot here the results obtained by SUnSAL$^{\mathrm{ASC}}$ but, instead, the results obtained by SUnSAL+ and CSUnSAL+ for white and correlated noise, respectively. Fig. 12 shows the values of SRE(dB) and $p_s$ for the two considered cases (white and correlated noise). These results exemplify the behavior of the constrained unmixing algorithms in the hypothetical situation in which the ASC constraint holds, which is an assumption that is not always true in real unmixing scenarios due to signature variability issues, as explained in Section II-A2. Fig. 12 shows that the performances of SUnSAL+ and FCLS are quite similar (with a small advantage for SUnSAL+) and generally superior to those achieved by CSUnSAL$^{\mathrm{ASC}}$ for white noise, while both CSUnSAL+ and CSUnSAL$^{\mathrm{ASC}}$ exhibit a significant performance improvement with regard to FCLS when applied to unmix observations affected by correlated noise, especially for high cardinalities of the solution.

### *G. Application of the Sparse Unmixing Techniques to the Image-Derived Endmembers*

The main goal of this experiment is to analyze the performance of sparse unmixing techniques when a spectral library is not available *a priori*. In this case, the proposed methods can still be applied by resorting to an artificially generated spectral library constructed using the image-derived endmembers. In our experiment, we first derived a subset of 12 members from library $\mathbf{A_1}$ (the subset was generated after retaining only the spectral signatures which form a spectral angle larger than 20° with all other signatures in the library). Then, we randomly selected five of the spectral signatures in the resulting subset and used them to generate a simulated hyperspectral image with 75 × 75 pixels and 224 bands per pixel. The data were generated using a linear mixture model, using the five randomly selected signatures as the endmembers and imposing the ASC in each simulated pixel. In the resulting image, shown in Fig. 13(a), there are pure regions as well as mixed regions constructed using mixtures ranging between two abd five endmembers, distributed spatially in the form of distinct square regions. Fig. 13(b)–(e), respectively, shows the true fractional abundances for each of the five endmembers. The background pixels are made up of a mixture of the same five endmembers, but this time, their respective fractional abundance values were fixed to 0.5130, 0.1476, 0.1158, 0.1242, and 0.0994, respectively. The simulated data were then contaminated with noise (SNR $= 20$ dB).

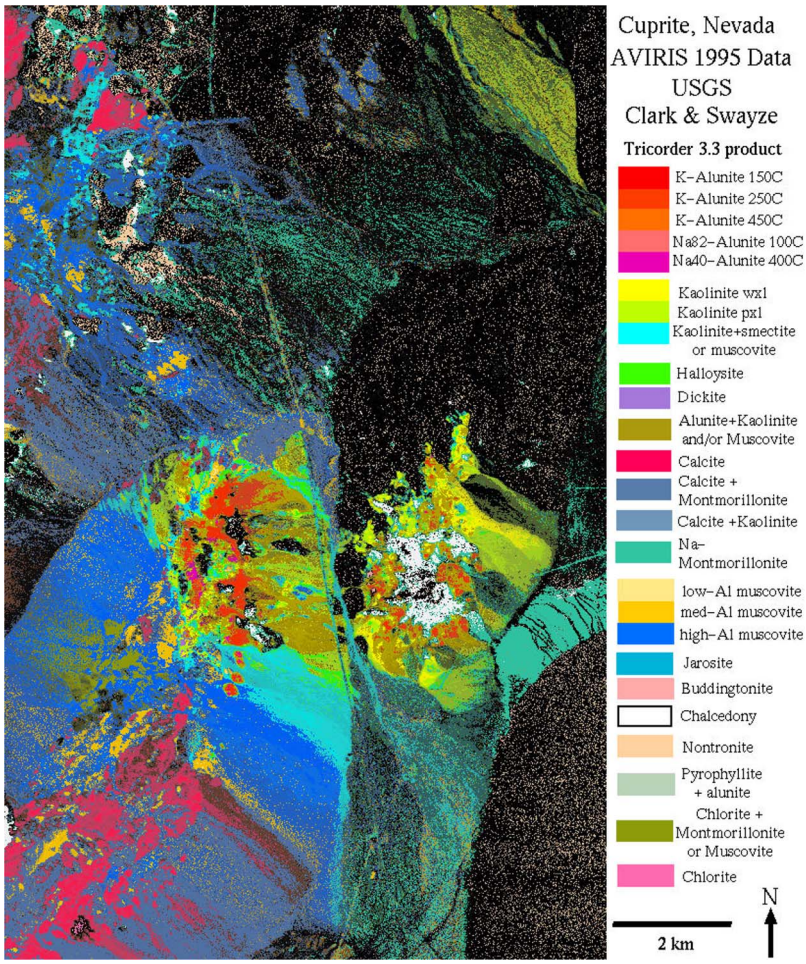


Fig. 15. USGS map showing the location of different minerals in the Cuprite mining district in NV. The map is available online at http://speclab.cr.usgs.gov/cuprite95.tgif.2.2um_map.gif.

Once the simulated data set was generated, we used the HySime algorithm [45] to find the signal subspace and projected the data on this subspace. Then, two endmember extraction algorithms (VCA and N-FINDR) were used to automatically extract the endmembers from the simulated data. The obtained endmember sets were merged in order to construct the spectral library used in the sparse unmixing process. In this library, only materials with a spectral angle of at least $3^\circ$ with regard to other materials in the library were retained in order to avoid strong similarities between the spectral signatures when conducting the sparse unmixing process. Abundance estimation was then conducted with SUnSAL+ using different values of the parameter $\lambda$. The same algorithm was used to find the NCLS solution by setting $\lambda = 0$. Finally, the estimated and true abundances were aligned, and the SRE(dB) was computed. Table II shows the mean SRE(dB) achieved both for different values of $\lambda$ and for each different endmember. For illustrative purposes, Fig. 14 also graphically shows the abundance estimation results obtained for one specific endmember (the fifth one used in the simulations). In Table II, it can be seen that the sparse techniques can still be successfully applied using the image-derived endmembers if in case there is no spectral library available *a priori*. Even in the presence of significant noise, SUnSAL+ always performed better than NCLS no matter what the value of $\lambda$ tested or the endmember considered is. The results shown in Fig. 14 are also in line with these observations. It is also worth noting that, in this experiment, we did not determine *a priori* the optimal parameter for $\lambda$.

### H. Summary and Main Observations

In summary, our main observation from the experiments conducted in this section is that the spectral libraries are indeed suitable in solving the sparse unmixing problem in our simulated analysis scenarios. Although the techniques which do not explicitly enforce the sparsity of the solution exhibit similar performances with regard to the sparse techniques when the observations are affected by white noise, our experimental results demonstrated that, by enforcing the sparsity of the solution, unmixing results can significantly improve when the observations are affected by correlated noise, which is the most typical one in real hyperspectral imaging scenarios. It is also worth noting that, according to our experiments, the sparse techniques exhibit not only a better performance when the number of endmembers is low (e.g., up to five), which is a reasonable assumption in practice, but also higher cardinalities when the noise is correlated. Finally, we also demonstrated that the sparse unmixing methods can be applied using the image-derived endmembers when there is no spectral library available *a priori*. Although our experiments with the simulated mixtures

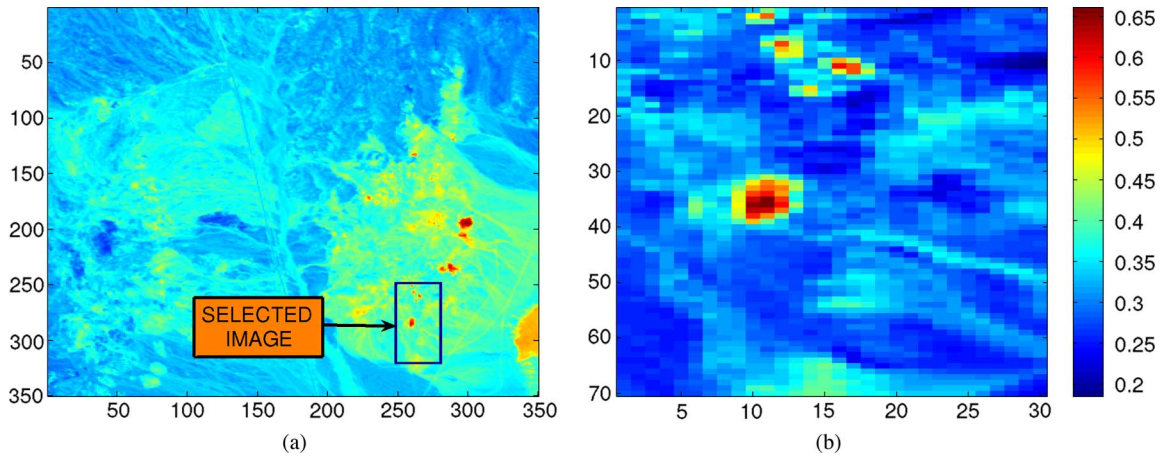


Fig. 16. AVIRIS Cuprite hyperspectral scene used in our experiments. (a) Spatial localization of a toy 70 × 30 pixel subscene in the considered 350 × 350 pixel data set. (b) Spectral band at the 558-nm wavelength of the toy subscene.

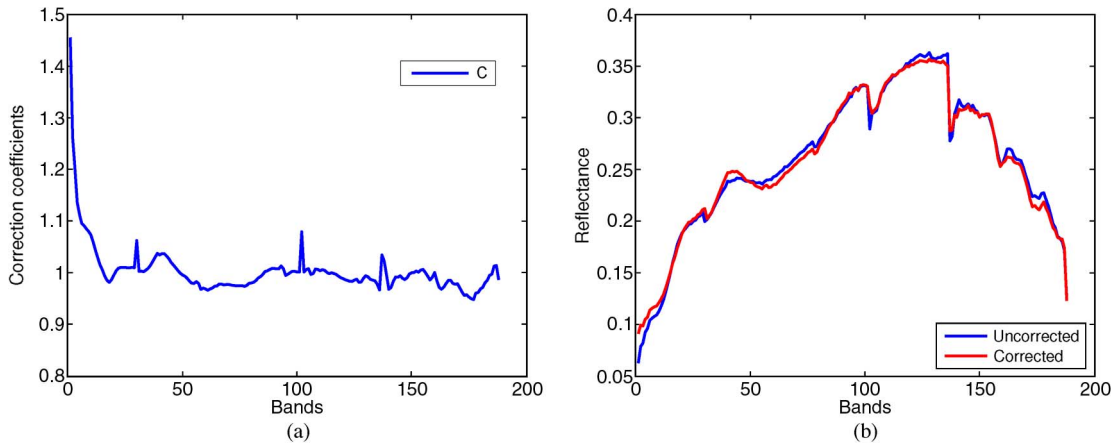


Fig. 17. (a) Plot of the diagonal values of correction matrix $\mathbf{C}$. (b) Original (blue) and corrected (red) spectra of a randomly selected pixel in the AVIRIS Cuprite data set.

are quite encouraging, the complexity of the real mixtures is usually quite high, and it is difficult to account for all possible issues affecting such mixtures when conducting simulations. For this reason, further experiments using real hyperspectral data sets are highly desirable. These will be conducted in the following section.

## V. Experiments With Real Data

The scene used in our real data experiments is the well-known AVIRIS Cuprite data set, available online in reflectance units.[6] This scene has been widely used to validate the performance of endmember extraction algorithms. The portion used in the experiments corresponds to a 350 × 350 pixel subset of the sector labeled as f970619t01p02_r02_sc03.a.rfl in the online data. The scene comprises 224 spectral bands between 0.4 and 2.5 $\mu$m, with a nominal spectral resolution of 10 nm. Prior to the analysis, bands 1–2, 105–115, 150–170, and 223–224 were removed due to water absorption and low SNR in those bands, leaving a total of 188 spectral bands. The Cuprite site is well understood mineralogically, and it has several exposed minerals of interest (all included in the USGS library considered in the experiments), denoted as splib06[7] and released in September 2007. In our experiments, we use the spectra obtained from this library as the input to the unmixing methods described in Section III. For illustrative purposes, Fig. 15 shows a mineral map produced in 1995 by USGS, in which the Tricorder 3.3 software product [46] was used to map different minerals present in the Cuprite mining district.[8] It should be noted that the Tricorder map is only available for the hyperspectral data collected in 1995, while the publicly available AVIRIS Cuprite data were collected in 1997. Therefore, a direct comparison between the 1995 USGS map and the 1997 AVIRIS data is not possible. However, the USGS map serves as a good indicator for the qualitative assessment of the fractional abundance maps produced by the unmixing algorithms described in Section III.

In order to compute the approximate solutions and to compare the performances of the algorithms described in Section III, a toy subscene of 70 × 30 pixels of the Cuprite data set was first used prior to conducting the experiments with

[6]http://aviris.jpl.nasa.gov/html/aviris.freedata.html.

[7]http://speclab.cr.usgs.gov/spectral.lib06.

[8]http://speclab.cr.usgs.gov/cuprite95.tgif.2.2um_map.gif.

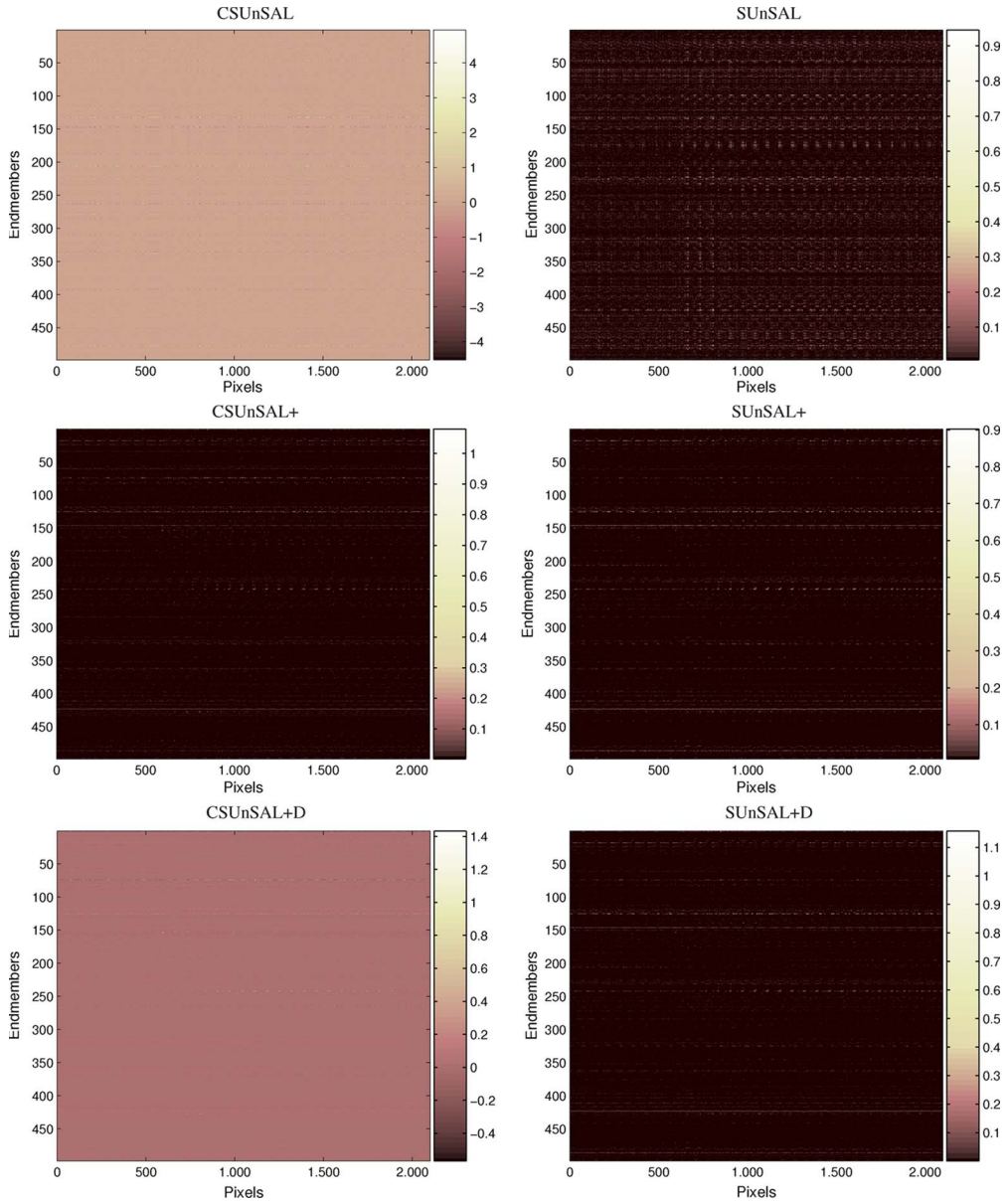


Fig. 18. Fractional abundance estimations obtained for each endmember material in the $\mathbf{A}_1$ spectral library (as a function of the pixel index in the considered toy subscene) by the considered sparse unmixing methods.

the 350 $\times$ 350 pixel scene. The position of the toy subscene in the 350 $\times$ 350 scene is shown in Fig. 16(a), while the spectral band at the 558-nm wavelength of the toy subscene is shown in Fig. 16(b). The results obtained for the 350 $\times$ 350 pixel scene are presented at the end of this section.

In all of our experiments with real data, we use library $\mathbf{A}_1$ to compute the approximate solutions. However, before processing the hyperspectral data, we should first focus our attention on the calibration issues. As we have already referred to before, even though we are working with atmospherically corrected data in reflectance units, there are always calibration mismatches between the real pixel spectra and the spectra available in the library due to the rather different acquisition conditions of the two data types. In order to minimize these mismatches, we apply a band-dependent correction strategy to the original data set, which amounts at replacing the data set

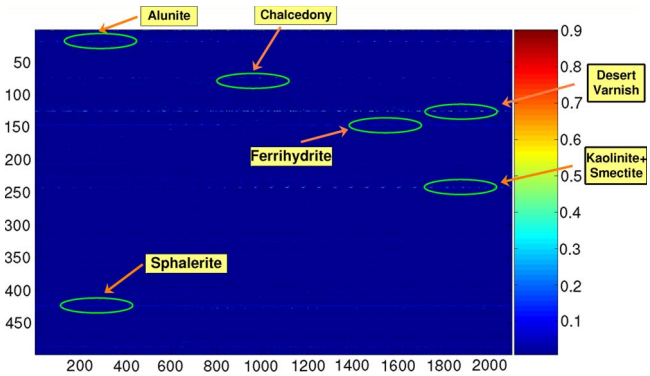


Fig. 19. Fractional abundance estimations obtained for each endmember material in the $\mathbf{A}_1$ spectral library (as a function of the pixel index in the considered toy subscene) by the SUnSAL+ method. The most significant minerals found by this algorithm are outlined.

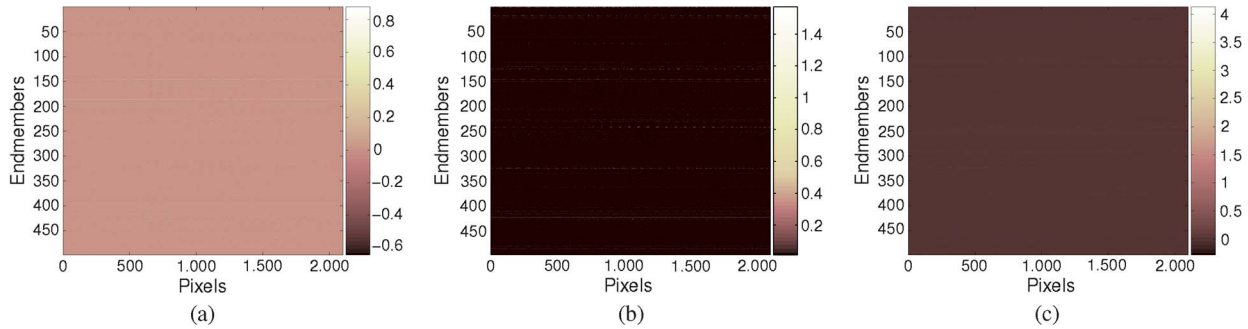


Fig. 20. Fractional abundance estimations obtained for each endmember material in the $\mathbf{A}_1$ spectral library (as a function of the pixel index in the considered toy subscene) by the OMP, OMP+, and ISMA methods. (a) OMP. (b) OMP+. (c) ISMA.

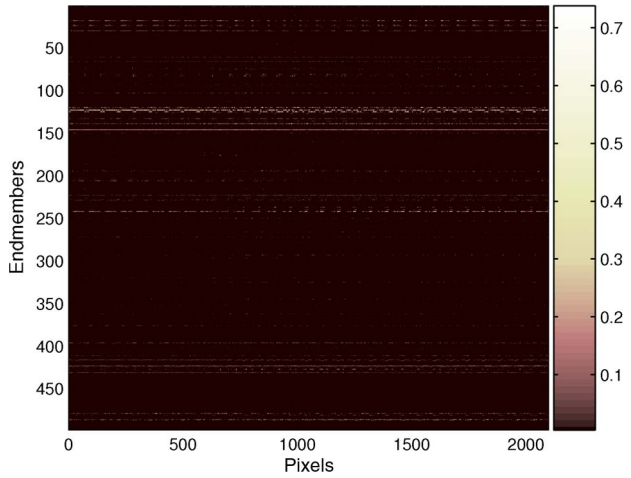


Fig. 21. Fractional abundance estimations obtained for each endmember material in the $\mathbf{A}_1$ spectral library (as a function of the pixel index in the considered toy subscene) by the NCLS method.

$\mathbf{Y}$ with $\mathbf{CY}$, where $\mathbf{C}$ is a diagonal matrix that minimizes the modeling error, i.e.,

$$\widehat{\mathbf{C}} = \arg \min_{\mathbf{C},\mathbf{X}\geq\mathbf{0},\mathbf{1}_m^T\mathbf{X}=\mathbf{1}_n^T} \|\mathbf{A}_1\mathbf{X} - \mathbf{CY}\|_2 \qquad (27)$$

where $\mathbf{X} \geq \mathbf{0}$ is the fractional abundance matrix. Problem (27) is nonconvex and, thus, very hard to exactly solve. We have computed a suboptimal solution to this problem by alternating the minimizing with respect to $\mathbf{C}$ and $\mathbf{X}$. We start the iterative procedure with $\mathbf{C} = \mathbf{I}$. The minimizations with respect to $\mathbf{C}$ and $\mathbf{X}$ are, respectively, the LS and constrained LS problems. To speed up the process and to ensure quality in the estimate of $\mathbf{C}$, we removed the nonsparse fractional abundances from $\mathbf{X}$ and the respective spectral vectors from $\mathbf{Y}$ after the first iteration. We ran a total of 20 iterations. The plot of the correction factors with regard to the spectral bands is shown in Fig. 17(a). These factors are always close to one, apart from a few bands in the blue wavelengths. For illustrative purposes, Fig. 17(b) shows a random pixel observation from the original AVIRIS Cuprite data set and its corrected version using the aforementioned strategy.

After correcting the data, the unmixing problem was first solved for the toy subscene using the sparse unmixing algorithms described in Section III. The parameters used were the following: $\lambda = 10^{-5}$ for SUnSAL and all its variations and $\delta = 10^{-4}$ for CSUnSAL and all its variations. Fig. 18 shows the fractional abundance estimations obtained for each endmember material in the $\mathbf{A}_1$ spectral library (as a function of the pixel index in the considered toy subscene) by the considered sparse unmixing methods. We emphasize that there are a total of $70 \times 30 = 2100$ pixels in the toy subscene. As shown in Fig. 18, the unconstrained version of CSUnSAL leads to highly inaccurate (i.e., physically unrealistic) results since the solutions contain negative values. CSUnSAL+, on the other hand, introduces more reasonable abundance estimates which, in turn, do not comply with the ASC constraint since the sum of all abundance fractions per pixel generally exceeds the value of 1.0, i.e., these are superunitary. $CSUnSAL + \mathrm{D}$ seems far more realistic than the unconstrained version. Both SUnSAL + D and CSUnSAL + D produce, in some cases, superunitary fractional abundances. SUnSAL and SUnSAL+ exhibit similar performances, with the general observation that SUnSAL returns vectors of fractional abundances which are more dense than SUnSAL+. Another general observation is that the constrained methods clearly show the sparsity of the solution as the nonzero fractions appear in distinct lines (sometimes grouped in clusters). This is due to the fact that, in the library, there are consecutive members describing similar materials. This general observation is strengthened if we compute the average number of endmembers having fractional abundances higher than 0.05 in one pixel: 44.05 for SUnSAL, 6.07 for SUnSAL+, 6.2 for SUnSAL + D, 68.55 for CSUnSAL, 8.36 for CSUnSAL+, and 11.09 for CSUnSAL + D. For illustrative purposes, Fig. 19 shows the most significant minerals found by SUnSAL+ in the toy subscene.

It is important to note that the constrained results of the sparse unmixing algorithms have very similar norms of the reconstruction error, with all of them situated for one randomly selected pixel around 0.05. We have used this observation in order to set the stopping threshold in the OMP and OMP+ algorithms to this value (i.e., by forcing them to achieve exactly the same error). In the case of the ISMA, we empirically set the algorithm threshold to $t_3 = 2$ based on the observed rmse variation of a small number of randomly selected pixels (10). It is also worth noting that choosing a threshold for the ISMA is extremely difficult in this application since the rmse has a very smooth variation and since the critical iteration is very difficult to identify. For illustrative purposes, the unmixing results after using these three algorithms (OMP, OMP+, and

TABLE III
PROCESSING TIMES (IN SECONDS) MEASURED AFTER APPLYING THE CONSIDERED UNMIXING ALGORITHMS TO THE TOY 70 × 30 PIXEL SUBSCENE ON A DESKTOP PC EQUIPPED WITH AN INTEL CORE 2 DUO CPU (AT 2.33 GHz) AND 2 GB OF RAM MEMORY

| | OMP | OMP+ | NCLS | ISMA | SUnSAL | SUnSAL+ | SUnSAL+D | CSUnSAL | CSUnSAL+ | CSUnSAL+D |
|---|---|---|---|---|---|---|---|---|---|---|
| Time [s] | 71 | 76 | 413 | 50400 | 195 | 420 | 520 | 1011 | 1355 | 1402 |

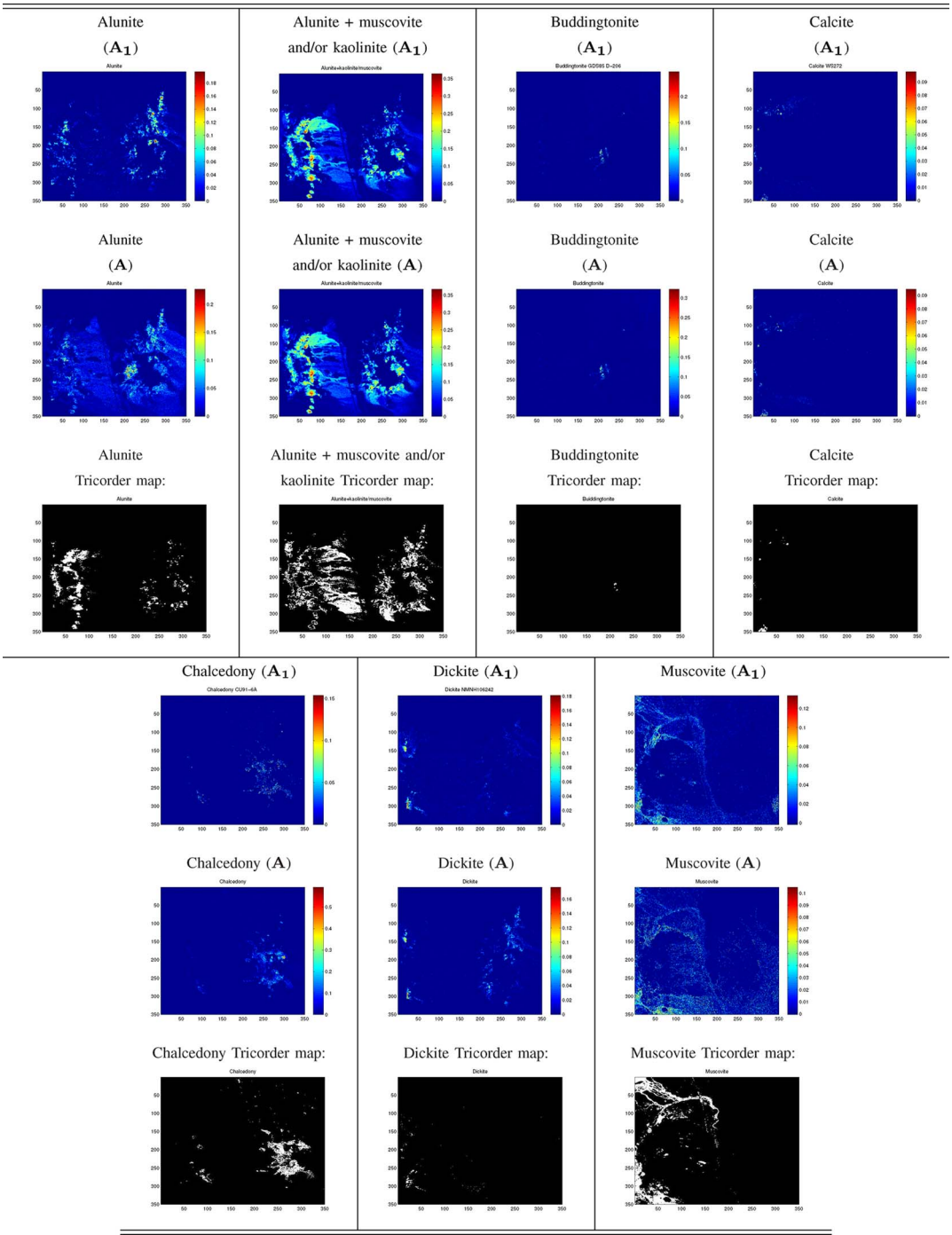


Fig. 22. Qualitative comparison between the fractional abundance maps estimated by the SUnSAL+ sparse unmixing technique and the classification maps produced by the USGS Tricorder algorithm for the 350 × 350 pixel AVIRIS Cuprite scene.

ISMA) are shown in Fig. 20. In Fig. 20, it can be seen that the OMP performs poorly (its solution contains many negative fractional abundances). OMP+ performs better and tolerates large superunitary values, although the sparsity of the solution is quite apparent. The same observation is valid for the ISMA. For the sake of completeness, Fig. 21 shows the fractional abundances estimated by the NCLS in the toy subscene. The results were obtained using the SUnSAL algorithm by setting

TABLE IV
PARAMETER SETTINGS USED IN OUR SIMULATED DATA EXPERIMENTS WHEN THE SNR WAS CONSTANT (SNR = 30 dB)

| | | $(a)$ White noise | | | $(b)$ Colored noise | | |
|---|---|---|---|---|---|---|---|
| | | $k_1 = 4$ | $k_2 = 10$ | $k_3 = 17$ | $k_1 = 4$ | $k_2 = 10$ | $k_3 = 17$ |
| | $\mathbf{A}_1$ | 0.31 | 0.29 | 0.23 | 0.045 | 0.02 | 0.005 |
| | $\mathbf{A}_2$ | 0.035 | 0.03 | 0.03 | 0.005 | 0.005 | 0.005 |
| OMP | $\mathbf{A}_3$ | 0.245 | 0.255 | 0.33 | 0.065 | 0.02 | 0.225 |
| $(t_1)$ | $\mathbf{A}_4$ | 0.105 | 0.02 | 0.02 | 0.315 | 0.005 | 0.01 |
| | $\mathbf{A}_5$ | 0.365 | 0.21 | 0.16 | 0.4 | 0.28 | 0.155 |
| | $\mathbf{A}_6$ | 0.29 | 0.25 | 0.24 | 0.275 | 0.225 | 0.07 |
| | $\mathbf{A}_1$ | 0.05 | 0.145 | 0.026 | 0.06 | 0.03 | 0.015 |
| | $\mathbf{A}_2$ | 0.21 | 0.02 | 0.02 | 0.005 | 0.005 | 0.005 |
| OMP+ | $\mathbf{A}_3$ | 0.02 | 0.085 | 0.245 | 0.275 | 0.155 | 0.165 |
| $(t_2)$ | $\mathbf{A}_4$ | 0.025 | 0.01 | 0.02 | 0.3 | 0.2 | 0.15 |
| | $\mathbf{A}_5$ | - | - | - | - | - | - |
| | $\mathbf{A}_6$ | 0.285 | 0.25 | 0.23 | 0.24 | 0.14 | 0.065 |
| | $\mathbf{A}_1$ | 0.04 | 0.004 | $7 \cdot 10^{-4}$ | $5 \cdot 10^{-4}$ | $5 \cdot 10^{-4}$ | $10^{-6}$ |
| | $\mathbf{A}_2$ | $10^{-4}$ | $4 \cdot 10^{-4}$ | $10^{-4}$ | $6 \cdot 10^{-4}$ | 0.001 | $5 \cdot 10^{-6}$ |
| ISMA | $\mathbf{A}_3$ | 0.003 | $10^{-4}$ | $5 \cdot 10^{-4}$ | 0.004 | 0.05 | $6 \cdot 10^{-4}$ |
| $(t_3)$ | $\mathbf{A}_4$ | $7 \cdot 10^{-4}$ | $7 \cdot 10^{-4}$ | $3 \cdot 10^{-4}$ | 0.03 | $2 \cdot 10^{-4}$ | $10^{-5}$ |
| | $\mathbf{A}_5$ | 0.03 | 0.001 | $10^{-4}$ | 0.03 | 0.001 | $10^{-4}$ |
| | $\mathbf{A}_6$ | 0.02 | 0.004 | 0.005 | 0.05 | $5 \cdot 10^{-4}$ | 0.004 |
| | $\mathbf{A}_1$ | 0.006 | 0.004 | 0.003 | $10^{-5}$ | $10^{-5}$ | $10^{-5}$ |
| | $\mathbf{A}_2$ | $3 \cdot 10^{-4}$ | $3 \cdot 10^{-4}$ | $6 \cdot 10^{-4}$ | $10^{-5}$ | $10^{-5}$ | $10^{-5}$ |
| SUNSAL | $\mathbf{A}_3$ | 0.4 | 0.5 | 0.5 | 0.008 | 0.003 | 0.001 |
| $(\lambda_1)$ | $\mathbf{A}_4$ | 0.002 | 0.003 | 0.004 | $5 \cdot 10^{-5}$ | $5 \cdot 10^{-5}$ | $10^{-5}$ |
| | $\mathbf{A}_5$ | 0.5 | 0.3 | 0.2 | 0.4 | 0.4 | 0.1 |
| | $\mathbf{A}_6$ | 0.5 | 0.3 | 0.5 | 0.4 | 0.2 | 0.1 |
| | $\mathbf{A}_1$ | 0.04 | 0.04 | 0.01 | $10^{-5}$ | $5 \cdot 10^{-5}$ | $5 \cdot 10^{-5}$ |
| | $\mathbf{A}_2$ | 0.005 | $10^{-6}$ | $10^{-5}$ | $10^{-5}$ | $10^{-6}$ | $5 \cdot 10^{-7}$ |
| SUNSAL+ | $\mathbf{A}_3$ | 0.5 | 0.3 | 0.4 | $5 \cdot 10^{-4}$ | $6 \cdot 10^{-4}$ | $5 \cdot 10^{-4}$ |
| $(\lambda_2)$ | $\mathbf{A}_4$ | $6 \cdot 10^{-5}$ | $5 \cdot 10^{-6}$ | $8 \cdot 10^{-5}$ | $10^{-4}$ | $10^{-5}$ | $10^{-5}$ |
| | $\mathbf{A}_5$ | 0.5 | 0.31 | 0.2 | 0.4 | 0.3 | 0.2 |
| | $\mathbf{A}_6$ | 0.08 | 0.06 | 0.07 | 0.04 | 0.03 | 0.3 |
| | $\mathbf{A}_1$ | 0.05 | 0.01 | 0.005 | $7 \cdot 10^{-4}$ | $3 \cdot 10^{-4}$ | $7 \cdot 10^{-4}$ |
| | $\mathbf{A}_2$ | 0.002 | $5 \cdot 10^{-4}$ | $10^{-5}$ | $3 \cdot 10^{-6}$ | $10^{-6}$ | $5 \cdot 10^{-7}$ |
| SUNSAL+D | $\mathbf{A}_3$ | 0.4 | 0.3 | 0.3 | 0.001 | 0.004 | 0.001 |
| $(\lambda_3)$ | $\mathbf{A}_4$ | 0.005 | 0.001 | 0.001 | $10^{-6}$ | $5 \cdot 10^{-6}$ | $10^{-7}$ |
| | $\mathbf{A}_5$ | - | - | - | - | - | - |
| | $\mathbf{A}_6$ | 0.1 | 0.1 | 0.3 | 0.09 | 0.09 | 0.09 |
| | $\mathbf{A}_1$ | 0.3 | 0.2 | 0.2 | 0.001 | 0.001 | $5 \cdot 10^{-4}$ |
| | $\mathbf{A}_2$ | 0.09 | 0.04 | 0.03 | $10^{-5}$ | $2 \cdot 10^{-4}$ | $10^{-4}$ |
| CSUNSAL | $\mathbf{A}_3$ | $10^{-7}$ | $10^{-7}$ | $10^{-12}$ | 0.03 | 0.02 | 0.009 |
| $(\delta_1)$ | $10^{-7}$ | 0.03 | 0.03 | 0.03 | $10^{-4}$ | $10^{-5}$ | $10^{-5}$ |
| | $\mathbf{A}_5$ | 0.3 | 0.2 | 0.1 | 0.3 | 0.1 | 0.08 |
| | $\mathbf{A}_6$ | 0.2 | 0.2 | 0.2 | 0.2 | 0.2 | 0.2 |
| | $\mathbf{A}_1$ | 0.4 | 0.3 | 0.3 | $10^{-5}$ | $5 \cdot 10^{-5}$ | $10^{-5}$ |
| | $\mathbf{A}_2$ | 0.03 | 0.03 | 0.03 | $10^{-4}$ | $10^{-4}$ | $5 \cdot 10^{-4}$ |
| CSUNSAL+ | $\mathbf{A}_3$ | 0.05 | 0.01 | 0.01 | $10^{-12}$ | $10^{-10}$ | $10^{-12}$ |
| $(\delta_2)$ | $\mathbf{A}_4$ | 0.03 | 0.03 | 0.02 | $10^{-5}$ | $5 \cdot 10^{-5}$ | $5 \cdot 10^{-5}$ |
| | $\mathbf{A}_5$ | 0.3 | 0.2 | 0.1 | 0.3 | 0.2 | 0.09 |
| | $\mathbf{A}_6$ | 0.2 | 0.2 | 0.2 | 0.3 | 0.2 | 0.1 |
| | $\mathbf{A}_1$ | 0.03 | 0.01 | 0.01 | $10^{-4}$ | $10^{-4}$ | $10^{-4}$ |
| | $\mathbf{A}_2$ | $10^{-4}$ | $10^{-5}$ | $10^{-5}$ | $10^{-4}$ | $10^{-5}$ | $10^{-5}$ |
| CSUNSAL+D | $\mathbf{A}_3$ | 0.002 | 0.002 | 0.001 | $10^{-4}$ | $10^{-4}$ | $10^{-4}$ |
| $(\delta_3)$ | $\mathbf{A}_4$ | $10^{-5}$ | $10^{-5}$ | $10^{-7}$ | $10^{-7}$ | $10^{-7}$ | $10^{-7}$ |
| | $\mathbf{A}_5$ | - | - | - | - | - | - |
| | $\mathbf{A}_6$ | 0.1 | 0.05 | 0.01 | 0.1 | 0.02 | 0.01 |

TABLE V
PARAMETER SETTINGS USED IN OUR SIMULATED DATA EXPERIMENTS WHEN THE SNR VARIED BETWEEN 20 AND 50 dB

| | | (a) White noise | | (b) Colored noise | |
|---|---|---|---|---|---|
| | | $k_1 = 25dB$ | $k_2 = 45dB$ | $k_1 = 25dB$ | $k_2 = 45dB$ |
| | $\mathbf{A}_1$ | 0.05 | 0.055 | 0.05 | 0.06 |
| | $\mathbf{A}_2$ | 0.055 | 0.09 | 0.05 | 0.05 |
| OMP | $\mathbf{A}_3$ | 0.05 | 0.05 | 0.05 | 0.05 |
| ($t_1$) | $\mathbf{A}_4$ | 0.05 | 0.05 | 0.05 | 0.05 |
| | $\mathbf{A}_5$ | 0.05 | 0.05 | 0.065 | 0.05 |
| | $\mathbf{A}_6$ | 0.05 | 0.05 | 0.05 | 0.055 |
| | $\mathbf{A}_1$ | 0.05 | 0.05 | 0.07 | 0.065 |
| | $\mathbf{A}_2$ | 0.05 | 0.05 | 0.05 | 0.05 |
| OMP+ | $\mathbf{A}_3$ | 0.05 | 0.05 | 0.05 | 0.05 |
| ($t_2$) | $\mathbf{A}_4$ | 0.05 | 0.05 | 0.05 | 0.05 |
| | $\mathbf{A}_5$ | - | - | - | - |
| | $\mathbf{A}_6$ | 0.05 | 0.05 | 0.05 | 0.055 |
| | $\mathbf{A}_1$ | $10^{-4}$ | $8 \cdot 10^{-5}$ | $8 \cdot 10^{-5}$ | $5 \cdot 10^{-5}$ |
| | $\mathbf{A}_2$ | $5 \cdot 10^{-5}$ | $5 \cdot 10^{-5}$ | $10^{-4}$ | $5 \cdot 10^{-5}$ |
| ISMA | $\mathbf{A}_3$ | $5 \cdot 10^{-5}$ | $10^{-4}$ | 0.2 | 0.05 |
| ($t_3$) | $\mathbf{A}_4$ | $5 \cdot 10^{-5}$ | $5 \cdot 10^{-5}$ | $8 \cdot 10^{-5}$ | $8 \cdot 10^{-5}$ |
| | $\mathbf{A}_5$ | 0.003 | $3 \cdot 10^{-4}$ | 0.005 | 0.001 |
| | $\mathbf{A}_6$ | 0.001 | $5 \cdot 10^{-5}$ | $5 \cdot 10^{-5}$ | $10^{-4}$ |
| | $\mathbf{A}_1$ | 0.05 | 0.001 | $10^{-5}$ | $10^{-5}$ |
| | $\mathbf{A}_2$ | 0.005 | $10^{-4}$ | $10^{-5}$ | $5 \cdot 10^{-5}$ |
| SUnSAL | $\mathbf{A}_3$ | 0.2 | 0.2 | 0.001 | $5 \cdot 10^{-5}$ |
| ($\lambda_1$) | $\mathbf{A}_4$ | $8 \cdot 10^{-4}$ | $10^{-4}$ | $10^{-5}$ | $10^{-5}$ |
| | $\mathbf{A}_5$ | 0.2 | 0.05 | 0.2 | 0.1 |
| | $\mathbf{A}_6$ | 0.2 | 0.05 | 0.2 | 0.01 |
| | $\mathbf{A}_1$ | 0.01 | $10^{-4}$ | 0.01 | $10^{-4}$ |
| | $\mathbf{A}_2$ | 0.005 | $10^{-4}$ | $10^{-8}$ | $5 \cdot 10^{-5}$ |
| SUnSAL+ | $\mathbf{A}_3$ | 0.2 | 0.2 | 0.01 | 0.003 |
| ($\lambda_2$) | $\mathbf{A}_4$ | $10^{-4}$ | $5 \cdot 10^{-5}$ | $10^{-4}$ | $10^{-5}$ |
| | $\mathbf{A}_5$ | 0.2 | 0.1 | 0.2 | 0.1 |
| | $\mathbf{A}_6$ | 0.2 | 0.05 | 0.05 | 0.01 |
| | $\mathbf{A}_1$ | 0.2 | 0.001 | 0.05 | 0.05 |
| | $\mathbf{A}_2$ | $10^{-4}$ | 0.2 | 0.001 | 0.2 |
| SUnSAL+D | $\mathbf{A}_3$ | 0.2 | 0.2 | 0.005 | $5 \cdot 10^{-5}$ |
| ($\lambda_2$) | $\mathbf{A}_4$ | 0.1 | 0.2 | 0.2 | 0.2 |
| | $\mathbf{A}_5$ | - | - | - | - |
| | $\mathbf{A}_6$ | 0.2 | 0.1 | 0.2 | 0.1 |
| | $\mathbf{A}_1$ | 0.3 | 0.05 | $8 \cdot 10^{-4}$ | $10^{-4}$ |
| | $\mathbf{A}_2$ | 0.05 | 0.005 | $10^{-8}$ | $10^{-8}$ |
| CSUnSAL | $\mathbf{A}_3$ | 0.3 | 0.3 | 0.01 | 0.001 |
| ($\delta_1$) | $\mathbf{A}_4$ | 0.05 | 0.005 | $5 \cdot 10^{-5}$ | $10^{-8}$ |
| | $\mathbf{A}_5$ | 0.3 | 0.05 | 0.3 | 0.05 |
| | $\mathbf{A}_6$ | 0.3 | 0.05 | 0.3 | 0.05 |
| | $\mathbf{A}_1$ | 0.3 | 0.05 | $8 \cdot 10^{-4}$ | $10^{-8}$ |
| | $\mathbf{A}_2$ | 0.05 | 0.005 | 0.003 | $10^{-4}$ |
| CSUnSAL+ | $\mathbf{A}_3$ | 0.3 | 0.3 | $10^{-8}$ | $5 \cdot 10^{-5}$ |
| ($\delta_2$) | $\mathbf{A}_4$ | 0.05 | 0.003 | $10^{-8}$ | $10^{-5}$ |
| | $\mathbf{A}_5$ | 0.3 | 0.05 | 0.3 | 0.05 |
| | $\mathbf{A}_6$ | 0.3 | 0.05 | 0.3 | 0.05 |
| | $\mathbf{A}_1$ | 0.3 | 0.05 | 0.1 | 0.05 |
| | $\mathbf{A}_2$ | 0.3 | 0.3 | 0.3 | 0.3 |
| CSUnSAL+D | $\mathbf{A}_3$ | 0.3 | 0.3 | $10^{-8}$ | $10^{-4}$ |
| ($\delta_3$) | $\mathbf{A}_4$ | 0.3 | 0.3 | 0.3 | 0.3 |
| | $\mathbf{A}_5$ | - | - | - | - |
| | $\mathbf{A}_6$ | 0.3 | 0.3 | 0.3 | 0.3 |

$\lambda = 0$ and by activating the ANC constraint. Before reporting the abundance estimation results obtained for the 350 $\times$ 350 pixel data set, Table III reports the processing times (in seconds) measured after applying the considered unmixing algorithms to the toy 70 $\times$ 30 pixel subscene. The algorithms were implemented using MATLAB R2009 on a desktop PC equipped with an Intel Core 2 Duo CPU (at 2.33 GHz) and 2 GB of RAM memory. As shown in Table III, the ISMA is quite slow compared to the other algorithms, while the OMP and OMP+ are the fastest ones. NCLS and SUnSAL in all its variants exhibit comparable running times, while CSUnSAL proves to be slower than them. In turn, SUnSAL is very fast in the unconstrained version. Although some of the reported sparse unmixing algorithms needed significant times to complete their calculations in this example, their implementation in the form of parallel algorithms is very feasible, and this strategy (not adopted in this paper) can lead to significant reductions in processing time in future developments.

Based on the previous results, which indicate that the ANC-constrained versions of SUnSAL and CSUnSAL exhibit similar performances in this problem and that the sparse techniques generally exhibit a better performance than those techniques that do not explicitly enforce sparseness, we now apply the SUnSAL+ algorithm to estimate the fractional abundances in the 350 $\times$ 350 pixel AVIRIS Cuprite scene using the spectral library $\mathbf{A_1}$ and a pruned version of $\mathbf{A_1}$. The pruned version was obtained by simply removing some of the spectral signatures which form a spectral angle smaller than 2.5°, thus obtaining a library with 390 spectrally distinct signatures denoted by $\mathbf{A}$. Fig. 22 shows a visual (qualitative) comparison between the fractional abundance maps, estimated for seven highly mixed materials in the AVIRIS Cuprite scene, by applying the SUnSAL+ algorithm. For comparative purposes, the spatial distribution maps of these materials extracted from the Tricorder classification map shown in Fig. 15 are also displayed. In Fig. 22, it can be observed that the SUnSAL+ sparse unmixing technique is able to find a good approximation for the distribution of the materials in the scene both for the original and pruned versions of the spectral library. It should be noted that there are still some differences between our estimated abundance maps and the Tricorder maps, mainly due to the fact that the Tricorder maps are, in fact, classification maps (i.e., all pixels are considered pure and are classified as members or not of a class given by the representative mineral in that pixel) and not abundance maps (in which the value assigned to a mixed pixel varies depending on the degree of presence of the mineral in the pixel). Even so, it can be visually seen that the SUnSAL+ sparse unmixing technique generally returns the highest abundances exactly for those pixels classified as members of the respective class of materials.

## VI. Conclusion and Future Research

In this paper, we have reformulated the spectral unmixing problem under the light of SR and have further evaluated the performance of several (available and new) SR algorithms in spectral unmixing applications. One significant advantage of using SR for spectral unmixing purposes is to take advantage of the increasing availability of the spectral libraries of the materials measured on the ground, e.g., using advanced field spectroradiometers. Through the sparse unmixing techniques described in this paper, mixed pixels can be expressed in the form of linear combinations of a number of pure spectral signatures known in advance and available in a library. With this strategy, the abundance estimation process no longer depends on the availability of pure spectral signatures in the input data nor on the capacity of a certain endmember extraction algorithm to identify such pure signatures. Being quite opposite, the procedure is reduced to finding the optimal subset of signatures in the library that can best model each mixed pixel in the scene.

Although our experimental results (conducted with both simulated and real data sets) are very encouraging, there are several aspects to be considered in practice, and they are worthy to be further investigated in future research efforts. One is the fact that the library spectra are rarely acquired under the same conditions as the airborne data. To address this issue, in this paper, we have adopted a simple correction algorithm to compensate for possible interferers. Another issue is the fact that the ability to obtain useful sparse solutions of an underdetermined system of equations mostly depends on the degree of coherence between the columns of the system matrix and also on the degree of sparseness of the original signals. As a result, the most favorable scenarios correspond to the highly sparse signals and system matrices with low coherence. Unfortunately, in hyperspectral imaging applications, the spectral signatures of the materials tend to be highly correlated. This unfavorable aspect is somehow balanced by the highly sparse nature of the fractional abundances. The final issue that is to be explored in future developments is the high computational complexity of the sparse unmixing algorithms, addressed in this paper by the consideration of the fast algorithms based on the augmented Lagrangian method of multipliers, but they are also subject to further improvements related to the inherently parallel nature of such algorithms. In fact, an important advantage of the sparse unmixing methods is that their complexity depends more on the cardinality of the solution and on the number of spectra in the library and less on the size of the hyperspectral image that is to be processed. Since the sparse unmixing is conducted in the pixel-by-pixel fashion, the procedure could be accelerated by dividing the image into subimages (or subsets of pixels) of any size and by processing the subpartitions in parallel without the need to establish an optimal size of subimages or subpartitions. This feature anticipates the high scalability of the potential parallel solutions to this approach.

## Appendix

In this Appendix, we report the parameters used in our simulated data experiments. Specifically, Table IV reports the parameters used when looking for the approximate solutions in the experiments with SNR = 30 dB for each considered cardinality, unmixing method, and spectral library. In order to ensure a fair comparison, we defined the near-optimal parameters for groups or levels of sparsity, with each group being described by a representative level for all considered methods. The parameters were denoted as follows: $t_1$, $t_2$, and $t_3$ are

the thresholds imposed on the stopping criteria for the OMP, OMP+, and ISMA; $\lambda_1$, $\lambda_2$, and $\lambda_3$ are the regularization parameters for SUnSAL, SUnSAL+, and SUnSAL + D; and $\delta_1$, $\delta_2$, and $\delta_3$ are the tolerance errors for CSUnSAL, CSUnSAL+, and CSUnSAL + D, respectively. It should be noted that the NCLS does not require any input parameter.

In order to find the near-optimal parameters in this particular case (SNR = 30 dB), the representative levels for the groups of sparsity were chosen as follows: for $k = 2, \ldots, 6$, the representative level is $k_1 = 4$; for $k = 7, \ldots, 13$, the representative level is $k_2 = 10$; and for $k = 14, \ldots, 20$, the representative level is $k_3 = 17$. Table IV [columns (a) and (b)] shows the near-optimal parameters established for the simulated data sets affected by white and correlated noise, respectively. These parameters are near optimal for the representative cardinalities, but they are applied for all sparsity levels in the respective group, and they were inferred by testing the algorithms using toy examples, i.e., by considering a large range of possible discrete values on the basis of a small number of samples (10).

On the other hand, Table V reports the parameters used in our simulated data experiments when the true cardinality was $k = 5$ and when the SNR varied between 20 and 50 dB. These parameters were found in a similar fashion to the ones reported in Table IV, considering two representative levels of the SNR: $k_1 = 25$ dB for SNR $= 20, \ldots, 30$ dB and $k_2 = 45$ dB for $k = 40, \ldots, 50$ dB. To conclude this section, we would like to emphasize our significant efforts in testing the most suitable parameters in order to report only the near-optimal results for each considered method.

## ACKNOWLEDGMENT

The authors would like to thank Dr. R.O. Green and Dr. R.N. Clark for, respectively, sharing the AVIRIS Cuprite data and the USGS spectral library with the scientific community and the Associate Editor and the three anonymous reviewers for their careful assessment of this paper and for their highly constructive suggestions in improving its technical quality and presentation.

## REFERENCES

[1] A. F. H. Goetz, G. Vane, J. E. Solomon, and B. N. Rock, "Imaging spectrometry for Earth remote sensing," *Science*, vol. 228, no. 4704, pp. 1147–1153, Jun. 1985.

[2] R. O. Green, M. L. Eastwood, C. M. Sarture, T. G. Chrien, M. Aronsson, B. J. Chippendale, J. A. Faust, B. E. Pavri, C. J. Chovit, M. Solis, M. R. Olah, and O. Williams, "Imaging spectroscopy and the Airborne Visible/Infrared Imaging Spectrometer (AVIRIS)," *Remote Sens. Environ.*, vol. 65, no. 3, pp. 227–248, Sep. 1998.

[3] D. A. Landgrebe, *Signal Theory Methods in Multispectral Remote Sensing*. New York: Wiley, 2003.

[4] C.-I. Chang, *Hyperspectral Imaging: Techniques for Spectral Detection and Classification*. New York: Kluwer, 2003.

[5] N. Keshava and J. F. Mustard, "Spectral unmixing," *IEEE Signal Process. Mag.*, vol. 19, no. 1, pp. 44–57, Jan. 2002.

[6] J. B. Adams, M. O. Smith, and P. E. Johnson, "Spectral mixture modeling: A new analysis of rock and soil types at the Viking Lander 1 site," *J. Geophys. Res.*, vol. 91, no. B8, pp. 8098–8112, 1986.

[7] D. C. Heinz and C.-I. Chang, "Fully constrained least squares linear mixture analysis for material quantification in hyperspectral imagery," *IEEE Trans. Geosci. Remote Sens.*, vol. 39, no. 3, pp. 529–545, Mar. 2001.

[8] J. M. P. Nascimento and J. M. Bioucas-Dias, "Does independent component analysis play a role in unmixing hyperspectral data?" *IEEE Trans. Geosci. Remote Sens.*, vol. 43, no. 11, pp. 75–187, Jan. 2005.

[9] A. Plaza, P. Martinez, R. Perez, and J. Plaza, "A quantitative and comparative analysis of endmember extraction algorithms from hyperspectral data," *IEEE Trans. Geosci. Remote Sens.*, vol. 42, no. 3, pp. 650–663, Mar. 2004.

[10] A. Plaza and C.-I. Chang, "Impact of initialization on design of endmember extraction algorithms," *IEEE Trans. Geosci. Remote Sens.*, vol. 44, no. 11, pp. 3397–3407, Nov. 2006.

[11] J. W. Boardman, F. A. Kruse, and R. O. Green, "Mapping target signatures via partial unmixing of AVIRIS data," in *Proc. JPL Airborne Earth Sci. Workshop*, 1995, pp. 23–26.

[12] M. E. Winter, "N-FINDR: An algorithm for fast autonomous spectral end-member determination in hyperspectral data," in *Proc. SPIE Imaging Spectrometry V*, 2003, vol. 3753, pp. 266–275.

[13] H. Ren and C.-I. Chang, "Automatic spectral target recognition in hyperspectral imagery," *IEEE Trans. Aerosp. Electron. Syst.*, vol. 39, no. 4, pp. 1232–1249, Oct. 2003.

[14] J. M. P. Nascimento and J. M. Bioucas-Dias, "Vertex component analysis: A fast algorithm to unmix hyperspectral data," *IEEE Trans. Geosci. Remote Sens.*, vol. 43, no. 4, pp. 898–910, Apr. 2005.

[15] J. H. Bowles, P. J. Palmadesso, J. A. Antoniades, M. M. Baumback, and L. J. Rickard, "Use of filter vectors in hyperspectral data analysis," in *Proc. SPIE Infrared Spaceborne Remote Sens. III*, 1995, vol. 2553, pp. 148–157.

[16] A. Ifarraguerri and C.-I. Chang, "Multispectral and hyperspectral image analysis with convex cones," *IEEE Trans. Geosci. Remote Sens.*, vol. 37, no. 2, pp. 756–770, Mar. 1999.

[17] R. A. Neville, K. Staenz, T. Szeredi, J. Lefebvre, and P. Hauff, "Automatic endmember extraction from hyperspectral data for mineral exploration," in *Proc. 21st Can. Symp. Remote Sens.*, 1999, pp. 21–24.

[18] A. Plaza, P. Martinez, R. Perez, and J. Plaza, "Spatial/spectral endmember extraction by multidimensional morphological operations," *IEEE Trans. Geosci. Remote Sens.*, vol. 40, no. 9, pp. 2025–2041, Sep. 2002.

[19] M. Berman, H. Kiiveri, R. Lagerstrom, A. Ernst, R. Dunne, and J. F. Huntington, "ICE: A statistical approach to identifying endmembers in hyperspectral images," *IEEE Trans. Geosci. Remote Sens.*, vol. 42, no. 10, pp. 2085–2095, Oct. 2004.

[20] L. Miao and H. Qi, "Endmember extraction from highly mixed data using minimum volume constrained nonnegative matrix factorization," *IEEE Trans. Geosci. Remote Sens.*, vol. 45, no. 3, pp. 765–777, Mar. 2007.

[21] D. M. Rogge, B. Rivard, J. Zhang, A. Sanchez, J. Harris, and J. Feng, "Integration of spatial–spectral information for the improved extraction of endmembers," *Remote Sens. Environ.*, vol. 110, no. 3, pp. 287–303, Oct. 2007.

[22] A. Zare and P. Gader, "Sparsity promoting iterated constrained endmember detection for hyperspectral imagery," *IEEE Geosci. Remote Sens. Lett.*, vol. 4, no. 3, pp. 446–450, Jul. 2007.

[23] J. Li and J. M. Bioucas-Dias, "Minimum volume simplex analysis: A fast algorithm to unmix hyperspectral data," in *Proc. IEEE IGARSS*, Jul. 2008, vol. 3, pp. III–250–III–253.

[24] J. M. Bioucas-Dias, "A variable splitting augmented Lagrangian approach to linear spectral unmixing," in *Proc. 1st WHISPERS*, Aug. 2009, pp. 1–4.

[25] A. Bruckstein, M. Elad, and M. Zibulevsky, "On the uniqueness of nonnegative sparse solutions to underdetermined systems of equations," *IEEE Trans. Inf. Theory*, vol. 54, no. 11, pp. 4813–4820, Nov. 2008.

[26] A. M. Bruckstein, D. L. Donoho, and M. Elad, "From sparse solutions of systems of equations to sparse modeling of signals and images," *SIAM Rev.*, vol. 51, no. 1, pp. 34–81, Feb. 2009.

[27] E. J. Candes and T. Tao, "Decoding by linear programming," *IEEE Trans. Inf. Theory*, vol. 51, no. 12, pp. 4203–4215, Dec. 2005.

[28] E. Candès, J. Romberg, and T. Tao, "Stable signal recovery from incomplete and inaccurate measurements," *Commun. Pure Appl. Math.*, vol. 59, no. 8, pp. 1207–1223, Aug. 2006.

[29] J. Bioucas-Dias and M. Figueiredo, Alternating Direction Algorithms for Constrained Sparse Regression: Application to Hyperspectral Unmixing, 2010, Arxiv preprint arXiv:1002.4527.

[30] D. L. Donoho and M. Elad, "Optimal sparse representation in general (non-orthogonal) dictionaries via l1 minimization," *Proc. Nat. Acad. Sci.*, vol. 100, no. 5, pp. 2197–2202, Mar. 2003.

[31] I. Gorodnitsky and B. Rao, "Sparse signal reconstruction from limited data using FOCUSS: A re-weighted minimum norm algorithm," *IEEE Trans. Signal Process.*, vol. 45, no. 3, pp. 600–616, Mar. 1997.

[32] B. Natarajan, "Sparse approximate solutions to linear systems," *SIAM J. Comput.*, vol. 24, no. 2, pp. 227–234, Apr. 1995.

[33] Y. C. Pati, R. Rezaiifar, and P. Krishnaprasad, "Orthogonal matching pursuit: Recursive function approximation with applications to wavelet decomposition," in *Proc. 27th Annu. Asilomar Conf. Signals, Syst., Comput.*, Los Alamitos, CA, 1993, pp. 40–44.
[34] S. Chen, D. Donoho, and M. Saunders, "Atomic decomposition by basis pursuit," *SIAM Rev.*, vol. 43, no. 1, pp. 129–159, 2001.
[35] S. Foucart and M. Lai, "Sparsest solutions of underdetermined linear systems via lq-minimization for 0," *Appl. Comput. Harmon. Anal.*, vol. 26, no. 3, pp. 395–407, May 2009.
[36] J. Tropp and A. Gilbert, "Signal recovery from random measurements via orthogonal matching pursuit," *IEEE Trans. Inf. Theory*, vol. 53, no. 12, pp. 4655–4666, Dec. 2007.
[37] C. Bateson, G. Asner, and C. Wessman, "Endmember bundles: A new approach to incorporating endmember variability into spectral mixture analysis," *IEEE Trans. Geosci. Remote Sens.*, vol. 38, pt. 2, no. 2, pp. 1083–1094, Mar. 2000.
[38] D. Donoho, M. Elad, and V. Temlyakov, "Stable recovery of sparse overcomplete representations in the presence of noise," *IEEE Trans. Inf. Theory*, vol. 52, no. 1, pp. 6–18, Jan. 2006.
[39] J. Tropp, "Just relax: Convex programming methods for subset selection and sparse approximation," Univ. Texas, Austin, TX, ICES Rep. 04-04, 2004.
[40] J. Eckstein and D. Bertsekas, "On the Douglas–Rachford splitting method and the proximal point algorithm for maximal monotone operators," *Math. Program.*, vol. 55, no. 3, pp. 293–318, Jun. 1992.
[41] M. Figueiredo, J. M. Bioucas-Dias, and M. Afonso, "Fast frame-based image deconvolution using variable splitting and constrained optimization," *Proc. 15th IEEE/SP Workshop SSP*, pp. 109–112, 2009.
[42] M. Afonso, J. M. Bioucas-Dias, and M. Figueiredo, "A fast algorithm for the constrained formulation of compressive image reconstruction and other linear inverse problems," in *Proc. IEEE ICASSP*, Dallas, TX, Mar. 2010, pp. 4034–4037.
[43] Z. Guo, T. Wittman, and S. Osher, "L1 unmixing and its application to hyperspectral image enhancement," in *Proc. SPIE Conf. Algorithms Technol. Multispectral, Hyperspectral, Ultraspectral Imaging XV*, Orlando, FL, 2009, p. 733 41M.
[44] D. M. Rogge, B. Rivard, J. Zhang, and J. Feng, "Iterative spectral unmixing for optimizing per-pixel endmember sets," *IEEE Trans. Geosci. Remote Sens.*, vol. 44, no. 12, pp. 3725–3736, Dec. 2006.
[45] J. M. P. Nascimento and J. M. Bioucas-Dias, "Hyperspectral subspace identification," *IEEE Trans. Geosci. Remote Sens.*, vol. 46, no. 8, pp. 2435–2445, Aug. 2008.
[46] R. N. Clark, G. A. Swayze, K. E. Livo, R. F. Kokaly, S. J. Sutley, J. B. Dalton, R. R. McDougal, and C. A. Gent, "Imaging spectroscopy: Earth and planetary remote sensing with the USGS Tetracorder and expert systems," *J. Geophys. Res.*, vol. 108, no. E12, p. 5131, 2003.

**Marian-Daniel Iordache** received the M.Sc. degree from the Faculty of Electrical Engineering, Politehnica University of Bucharest, Bucharest, Romania, in July 2006. He is currently working toward the Ph.D. degree at the Instituto Superior Técnico (IST), Lisbon, Portugal.

His research activity started in 2006 at the Electrical Engineering Research Center, Bucharest, where he worked on several national and European projects dedicated to microelectromechanical systems and high-frequency circuits. In 2008, he was a Marie Curie fellow with the Hyperspectral Imaging Network project funded by the European Commission under the Sixth Framework Programme. He is currently carrying out his research as a member of the HyperComp research group at the University of Extremadura (UEX), Cáceres, Spain, under the joint supervision of Prof. J.M. Bioucas-Dias (IST) and Prof. A. Plaza (UEX). His research is focused on hyperspectral unmixing, with emphasis on the sparse characteristics of the solutions.

**José M. Bioucas-Dias** (S'87–M'95) received the E.E., M.Sc., Ph.D., and "Agregado" degrees from the Technical University of Lisbon, Lisbon, Portugal, in 1985, 1991, 1995, and 2007, respectively, all in electrical and computer engineering.

Since 1995, he has been with the Department of Electrical and Computer Engineering, IST. He is also a Senior Researcher with the Communication Theory and Pattern Recognition Group, Telecommunications Institute, which is a private not-for-profit research institution. He is involved in several national and international research projects and networks, including the Marie Curie Actions "Hyperspectral Imaging Network" and the "European Doctoral Program in Signal Processing (SIGNAL)." His research interests include signal and image processing, pattern recognition, optimization, and remote sensing.

Dr. Bioucas-Dias is an Associate Editor of the IEEE TRANSACTIONS ON IMAGE PROCESSING, and he was an Associate Editor of the IEEE TRANSACTIONS ON CIRCUITS AND SYSTEMS and a Guest Editor of a special issue of the IEEE TRANSACTIONS ON GEOSCIENCE AND REMOTE SENSING. He has been a member of program/technical committees of several international conferences, including Computer Vision and Pattern Recognition, International Conference on Pattern Recognition, International Conference on Image Analysis and Recognition, International Geoscience and Remote Sensing Symposium, International Conference on Image Processing, International Society for Optics and Photonics, International Conference on Energy Minimization Methods in Computer Vision and Pattern Recognition, International Symposium on Visual Computing, and Workshop on Hyperspectral Image and Signal Processing: Evolution in Remote Sensing.

**Antonio Plaza** (M'05–SM'07) received the M.S. and Ph.D. degrees in computer engineering from the University of Extremadura (UEX), Cáceres, Spain, in 1997 and 2002, respectively.

He was a Visiting Researcher with the Remote Sensing Signal and Image Processing Laboratory, University of Maryland Baltimore County, Baltimore; with the Applied Information Sciences Branch, Goddard Space Flight Center, Greenbelt, MD; and with the AVIRIS Data Facility, Jet Propulsion Laboratory, Pasadena, CA. Since 2000, he has been an Associate Professor with the Department of Technology of Computers and Communications, UEX, where he was an Assistant Professor from 1997 to 1999. He is the Coordinator of the Hyperspectral Imaging Network, which is a European project designed to build an interdisciplinary research community focused on hyperspectral imaging activities. He is a Proposal Reviewer with the European Commission, the European Space Agency, and the Spanish Government, and he has also served as a Reviewer for more than 40 different journals. He is the author or coauthor of more than 230 publications on remotely sensed hyperspectral imaging, including more than 40 journal citation report papers, book chapters, and conference proceeding papers. He has coedited a book on high-performance computing in remote sensing and several special issues on remotely sensed hyperspectral imaging for different journals. His research interests include remotely sensed hyperspectral imaging, pattern recognition, signal and image processing, and efficient implementation of large-scale scientific problems on parallel and distributed computer architectures.

Dr. Plaza is an Associate Editor of the IEEE TRANSACTIONS ON GEOSCIENCE AND REMOTE SENSING on hyperspectral image analysis and signal processing, where he has served as a Reviewer for more than 130 manuscripts. He was a recipient of the recognition of Best Reviewers of the IEEE GEOSCIENCE AND REMOTE SENSING LETTERS in 2009.